



1 **Role of atmospheric horizontal resolution in simulating**
2 **tropical and subtropical South American precipitation in**
3 **HadGEM3-GC31**

4 Paul-Arthur Monerie¹, Amulya Chevuturi¹, Peter Cook¹, Nick Klingaman¹, Christopher E. Holloway²

5

6 ¹Department of Meteorology, National Centre for Atmospheric Science (NCAS), University of
7 Reading, Reading, UK

8 ²Department of Meteorology, University of Reading, Reading, UK

9 *Correspondence to:* Paul-Arthur Monerie (pmonerie@gmail.com)

10

11 **Abstract**

12 We assess the effect of increasing horizontal resolution on simulated precipitation over South America in
13 a climate model. We use atmosphere-only simulations, performed with HadGEM3-GC31 at three horizontal
14 resolutions: N96 (~130 km, 1.88° x 1.25°), N216 (~60 km, 0.83° x 0.56°), and N512 (~25 km, 0.35° x
15 0.23°). We show that all simulations have systematic biases in annual mean and seasonal mean precipitation
16 over South America (e.g. too wet over the Amazon and too dry in northeast). Increasing horizontal
17 resolution improves simulated precipitation over the Andes and north-east Brazil. Over the Andes,
18 improvements from horizontal resolution continue to ~25km, while over north-east Brazil, there are no
19 improvements beyond ~60km resolution. These changes are primarily related to changes in atmospheric
20 dynamics and moisture flux convergence. Over the Amazon basin, precipitation variability increases at
21 higher resolution. We show that some spatial and temporal features of daily South American precipitation
22 are improved at high resolution, including the intensity spectra of rainfall. Spatial scales of daily



23 precipitation features are also better simulated, suggesting that higher resolution may improve the
24 representation of South American mesoscale convective systems.

25 **1. Introduction**

26

27 South America is a large area encompassing tropical, sub-tropical and extratropical climates. The Andes
28 covers western South America, from South to North, while the eastern part of South America is flatter than
29 the west. The Amazon basin has high mean rainfall and is covered by a rainforest, while northeastern Brazil
30 is semi-arid. Several climatic areas are thus often defined to account for the climatic heterogeneity of South
31 America, with focus specifically on the Andes, the Amazon Basin, north-east Brazil and south-east Brazil
32 (de Souza Custodio et al. 2017).

33 Climate models have biases in simulating South American precipitation, partly due to biases in simulating
34 teleconnections between both Atlantic and Pacific sea-surface temperatures (SSTs), and precipitation over
35 land (Bombardi and Carvalho 2008; Jung et al. 2011; Yin et al. 2013; Sierra et al. 2015; Coelho et al. 2016;
36 Koutroulis et al. 2016). At sub-seasonal scales, precipitation variability is associated with the Madden—
37 Julian Oscillation (MJO) (Grimm 2019). The MJO modulates precipitation over South America, leading to
38 either anomalously dry or wet conditions over South America, depending on its phase. The MJO also favors
39 extreme events, leading to droughts and floods (Grimm 2019). At inter-annual scales, the El Niño Southern
40 Oscillation (ENSO) strongly impacts Amazon precipitation, with El Niño events related to droughts
41 (Grimm and Silva Dias 1995; Zeng et al. 2008; Marengo et al. 2008, 2011, 2013; Grimm and Tedeschi
42 2009; Lewis et al. 2011). Variability in the tropical Atlantic Ocean modulates trade easterlies and impacts
43 precipitation over north-east Brazil (Liu and Juárez 2001; Zeng et al. 2008) and south-east Brazil (Coelho
44 et al. 2016). On decadal to multi-decadal scales, variability in north-east Brazilian precipitation is tied to
45 the Atlantic Multidecadal Variability, which is associated with the location of the Atlantic Intertropical
46 Convergence Zone (ITCZ) (Knight et al. 2006). Brazilian precipitation is also associated with Interdecadal



47 Pacific Variability (IPV; Power et al. 1999), positive IPV phases reduce precipitation over South America
48 (Villamayor et al. 2018). Errors in simulating teleconnections from local and remote SST variability leads
49 to biases in the intensity, position of the ITCZ and the South Atlantic Convergence Zone (SACZ), which
50 degrade simulated South American precipitation and temperature (Bombardi and Carvalho 2008; Custódio
51 et al. 2012; de Souza Custodio et al. 2017).

52 Besides teleconnections, climate variability results from complex local interactions between energy,
53 precipitation and soil moisture. These feedbacks are particularly strong over interior South America, one
54 of the “hot spots” in soil moisture—precipitation coupling (Koster et al. 2004; Wei and Dirmeyer 2012).
55 Variability in recycling accounts for a large fraction of precipitation variability over north-eastern Brazil
56 and the La Plata Basin (Sörensson and Menéndez 2011). Soil moisture memory influences atmospheric
57 variability and could affect the development of the South American Monsoon System. Therefore, biases in
58 simulated South American climate may be partly attributed to biases in local land-atmosphere coupling.

59 Improving simulated precipitation in climate models may also improve subseasonal-to-decadal predictions,
60 because the performance of initialised forecasts and free-running models relies on the representation of key
61 physical processes, such as convection and land-atmosphere feedbacks. For instance, models with the
62 largest systematic errors produce the lowest precipitation prediction performance (DeSole and Shukla
63 2010). Jia et al. (2014) showed that the high-resolution version of the GFDL model produces lower biases
64 and higher skill for seasonal variations of 2-m air temperature and precipitation over South America, than
65 its lower-resolution counterpart. Therefore, Doblas-Reyes et al. (2013) proposed that increasing spatial
66 resolution is one of the main challenges for improving predictions.

67 Horizontal resolutions of Coupled Model Intercomparison Project (CMIP; Taylor et al. 2012; Eyring et al.
68 2016) models are typically ~150 km, or coarser, in the atmosphere, and ~100 km in the ocean. Important
69 climate processes, such as atmospheric convection, and mesoscale boundary currents and eddies, have to
70 be parameterized rather than resolved, which may compromise dynamical processes and dynamics-physics



71 interactions (Collins et al. 2018). A growing body of evidence shows then that increasing horizontal
72 resolution can improve some aspects of the simulated climate (Roberts et al. 2018, 2019; among others).
73 Higher-resolution ocean-atmosphere coupled models outperform lower-resolution models at simulating
74 SST over coastal upwelling regions, due to a better simulation of near-surface wind and its effect on the
75 ocean (Shaffrey et al. 2009; Gent et al. 2010; McClean et al. 2011; Delworth et al. 2011; Sakamoto et al.
76 2012; Small et al. 2014). Resolution reduces the double ITCZ bias (Delworth et al. 2011) and improves
77 variability in the El-Niño Southern Oscillation (Shaffrey et al. 2009; Sakamoto et al. 2012; Small et al.
78 2014) and north Atlantic SSTs (Gent et al. 2010). Jung et al. (2011) and Jia et al. (2014) highlighted that
79 increased resolution improved simulated South American precipitation and tropical mean precipitation, and
80 atmospheric circulation. Improved land precipitation is partly due to a better representation of orography
81 (Gent et al. 2010; Delworth et al. 2011; Sakamoto et al. 2012). Over South America, increasing horizontal
82 resolution improves the representation of climate patterns (de Souza Custodio et al. 2017), particularly over
83 the Ocean, over the Atlantic ITCZ and SACZ. Although strongly model and season dependent, high
84 resolution regional climate models also improve simulated precipitation and temperature over South
85 America (Falco et al. 2019; Solman and Blázquez 2019). Increased resolution also affects local features,
86 such as the propagation of mesoscale systems (Vellinga et al. 2016) and local land-atmosphere feedbacks
87 (Mueller et al. under review).

88 However, horizontal resolution does not always improve simulated climate. Bacmeister et al. (2013) found
89 that the high-resolution Community Atmosphere Model (CAM) did not improve simulated South American
90 rainfall, compared to a lower-resolution configuration. Some simulations exhibit too much warming and
91 cooling, especially over polar regions where sea ice is not accurately represented (McClean et al. 2011;
92 Kirtman et al. 2012). Impacts of increased horizontal resolution strongly depend on the range of resolutions
93 considered, on the region, phenomena and spatial and temporal scales of interest (Jung et al. 2011; Roberts
94 et al. 2018). Therefore, there is a need to better understand how increasing the horizontal resolution could
95 benefit simulated South American precipitation.



96

97

98 Accurate predictions and projections of extreme rainfall require realistic simulated precipitation
99 distributions. However, models exhibit biases in the frequency and persistence of light ($<10 \text{ mm.day}^{-1}$) and
100 heavy precipitation ($>20 \text{ mm.day}^{-1}$) (Sun et al. 2006; Dai 2006; Koutroulis et al. 2016). Errors in
101 precipitation frequency and intensity are related to biases in the global hydrological cycle, including
102 evaporation recycling over land (Trenberth 2011; Demory et al. 2014). Improved representations of intense
103 small-scale events improves precipitation variability in models over parts of South America (De Sales and
104 Xue 2011). These biases may be partly due to the coarse resolution of CMIP climate models; increased
105 resolution could improve simulated extreme convective rainfall by enhancing smaller-scale precipitation
106 features, as shown by Solman and Blázquez (2019) over South America.

107 High resolution models are costly; if higher resolution produces little or no improvements in model biases,
108 then computational resources could be used elsewhere, such as in increased ensemble size or adding
109 initialization dates in forecasting systems, or improved or additional model physics. The European Union's
110 Horizon 2020 PRIMAVERA project (www.primavera-h2020.eu) uses the CMIP6 High Resolution Model
111 Intercomparison Project (HighResMIP; Haarsma et al. 2016) protocol and aims to develop a new generation
112 of advanced high-resolution global climate models.

113 We use PRIMAVERA simulations to evaluate whether increased horizontal resolution improves simulated
114 South American precipitation. We address three main questions:

115 - What are the model biases in simulated precipitation over South America?

116 - Is South American mean precipitation and variability better simulated at higher than at lower resolution?

117 What is the minimum resolution required to improve the lower resolution biases?

118 - Are the spatial and temporal organizations of precipitation, better simulated at higher resolution?



119 The paper is structured as follows: the model, data and methodology are described in Sect. 2. Sect. 3 focuses
120 on the model's ability to simulate annual and seasonal precipitation mean. We discuss seasonal to
121 interannual variability in Sect. 4 and daily to sub-seasonal variability and spatial and temporal scales of
122 precipitation in Sect. 5. A conclusion is given in Sect. 6.
123



124 **2. Data and Methods**

125 **2.1 HadGEM3-GC3.1**

126

127 HadGEM3-GC3.1 (hereafter HadGEM3) (Williams et al. 2018) has been run in an atmosphere-only
128 configuration for 1950-2014, forced by HadISST2 daily 0.25° SSTs and sea ice (Rayner et al. 2006). The
129 atmospheric model is the Global Atmosphere 7.1 scientific configuration (Walters et al. 2019), with 85
130 vertical levels. A common historical forcing is imposed in all simulations, including SSTs, greenhouse
131 gases and aerosols. Three sets of simulations are performed, which only differ by their horizontal resolution
132 and by a stochastic perturbation of their initial conditions: N96 horizontal resolution (~130 km, 1.88° x
133 1.25°; HadGEM3-GC3.1-LM), N216 horizontal resolution (~60 km, 0.83° × 0.56°; HadGEM3-GC3.1-
134 MM) and N512 horizontal resolution (~25 km, 0.35° x 0.23°; HadGEM3-GC3.1-HM). Three members
135 were performed at each resolution, for a total of 9 simulations.

136

137 **2.2 Observations and reanalysis**

138 To verify the spatial and temporal scales of rainfall, three-hour and daily mean precipitation from
139 HadGEM3 is compared against a high-resolution (0.25° x 0.25°) satellite-derived product for 1998-2017:
140 NOAA CPC Morphing Technique (CMORPH version 1; Joyce et al. 2004). To evaluate time-mean rainfall
141 and sub-seasonal to seasonal variability, we compare HadGEM3 to longer-period, but lower-resolution,
142 gauge-based datasets from the University of Delaware (Willmott et al. 2001) and from the Global
143 Precipitation Climatology Centre (GPCC; Schneider et al. 2014). We assess mean circulation against the
144 NCEP-NCAR reanalysis (Kanamitsu et al. 2002) and ERA-interim reanalysis (Dee et al. 2011).

145 To assess biases and impacts of the horizontal resolution on mean annual and seasonal precipitation we
146 used monthly data, over 1950-2014, using GPCC and ERA-interim. For daily variance we used GPCC,



147 over 1982-2014. For the analysis of the spatial scales in precipitation, we used CMORPH, over 1998-2014.
148 Note that results in mean and variance in precipitation were also assessed with CMORPH, in addition to
149 GPCC, for a consistency with the spatial scales analysis.

150 **2.3 Data interpolation**

151 Differences between HadGEM3 and observations and between HadGEM3 at different horizontal
152 resolutions are assessed by first interpolating all data to a common $0.5^\circ \times 0.5^\circ$ resolution. Results were
153 repeated, with data interpolated onto a common coarser resolution, $2.5^\circ \times 2.5^\circ$ grid, showing similar results.
154 For the analysis of the spatial scales in precipitation, both simulations and observations are interpolated
155 onto a common lower resolution, N96.

156 **2.4 Analysis of Scales of Precipitation (ASoP)**

157 The Analysis of Scales of Precipitation (ASoP; Klingaman et al. 2017; Martin et al. 2017) diagnostics
158 provide information on the intensity spectra of precipitation, the contribution to total precipitation from
159 precipitation events of various intensities, the temporal persistence of precipitation and the typical spatial
160 and temporal scales of precipitation.

161 The intensity spectra measures intensity distributions by computing the contributions of discrete intensity
162 bins to the total precipitation for each grid point, to be visualised as maps (at grid scale) or aggregated over
163 regions into histograms. Spatial scales of precipitation features are measured by dividing the analysis
164 domain into non-overlapping subregions and computing correlations of each point in the sub-region against
165 the central grid point, then averaging the resulting correlation maps over all sub-regions. Temporal scales
166 are measured by auto-correlations at a range of lags. Further information can be found in Klingaman et al.
167 (2017) and Martin et al. (2017).



168 Further, we measure the distribution of the duration of precipitation events in discrete intensity bins by
169 constructing a two-dimensional (2-D) histogram of binned precipitation intensity against binned duration
170 in that intensity bin. We calculate the 2-D histogram by aggregating data across the analysis domain, then
171 normalised by the number of spatial and temporal points in the dataset, to compare across datasets. The
172 ASoP and duration diagnostics are applied over two subregions of South America: Amazon (AMZ; 10°S –
173 5°N; 72°W – 50°W) and southeast South America (SESA; 35°S – 18°S; 63°W – 40°W). We apply these
174 diagnostics to daily data on the native HadGEM3 and CMORPH grids, as well as a common N96 grid.

175 We produce a 1-D histogram for duration of dry spells, where a dry spell is defined as a time interval of
176 consecutive precipitation events of less than 0.1 mm.day⁻¹. This histogram is normalized by number of
177 spatial and temporal points in the dataset, to compare across datasets.

178

179 **2.5 Coupling strength metric**

180 Interactions between soil moisture, precipitation, temperature and evaporation modulate climate variability.
181 We assess the sensitivity of coupling strength between these variables to resolution. Coupling strength is
182 defined, at each grid point, after removing the linear trend and seasonal cycle, and on the daily time scale,
183 as

$$184 \quad r_{a,b}\sigma_b = cor(a,b) \times std(b)$$

185 Where $cor(a,b)$ is the correlation between the variables a and b and std is the standard deviation. As an
186 example, for the coupling strength between soil moisture (in the top 0.1m of soil) and latent heat flux, a is
187 the soil moisture, and b is the latent heat flux. The linear trend was removed over all days, selecting DJF
188 months only, and across all years to define anomalies relative to the seasonal cycle. We only selected days
189 over the DJF season, between 1950 and 2014. The coupling strength is also computed with a 2-day lag
190 correlation.



191

192

193 **3 Interannual and seasonal means**

194 **3.1 interannual mean**

195 Observed annual mean precipitation is high over the equator, i.e. the Amazon Basin, Colombia and South
196 Venezuela, while eastern Brazil is relatively dry (Fig. 1a). Precipitation is stronger over the eastern side of
197 the Andes than over the western side, because moisture is carried across South America by the trade
198 easterlies. Over the Andes, peaks in precipitation are collocated with the orography.

199 HadGEM3 has clear deficiencies in simulating precipitation, particularly over high orography. N96 has a
200 wet bias over southern Brazil and over the Andes, from 30°S to the equator, and a dry bias over north-east
201 Brazil (Fig. 1b). Biases are strong, up to 3 mm.day⁻¹ over the Andes. The dry bias over the north-east Brazil
202 is associated with anomalously weak easterlies (Fig. 1b). An anomalously strong cyclonic circulation,
203 located over Peru, weakens the easterlies, between 10°S and the equator, decreasing moisture flux
204 divergence over the western Amazon Basin associated with a wet bias there (Fig. 1b). There is an
205 anomalously strong anticyclonic circulation, over south-east Brazil, which is associated with stronger
206 easterlies from the South Atlantic Ocean to southern Brazil and a wet bias (Fig. 1b).

207

208 N216 and N512 also show, wet biases over the Andes and south-eastern Brazil, and dry biases over north-
209 east Brazil (Fig. 1c and Fig. 1d). Biases in low-level winds are also very similar in N96, N216 and N512.
210 We highlight the impacts of each step change in resolution by displaying differences between all pairs of
211 simulations. The total impact of shifting from N96 to N512 is given by N512-N96; intermediate steps are
212 illustrated by N216-N96 and N512-N216. This helps to define the minimum resolution required to extract
213 substantial simulation improvements, from the available sets of simulations. The strongest impact of
214 increasing resolution is over the Andes, where N512-N96 reaches up to 2 mm.day⁻¹ (Fig. 2c). Significant
215 differences are also obtained over the Amazon Basin, north-east Brazil and north-west Argentina (Fig. 2a-



216 c). Over the Amazon basin and the Andes, changes in precipitation in N512-N96 are due to both N216-N96
217 and N512-N216 (Fig. 2a and Fig. 2b). In addition, differences consist of reduced precipitation (Fig. 2abc),
218 and thus in reduced wet biases, over the Andes (Fig. 1bcd; see the stippling). Therefore, it is worth
219 increasing horizontal resolution to N512 for simulating precipitation over the Andes.

220
221 Over northern Argentina, significant changes are only due to N216-N96 (Fig. 2a), while there are no
222 significant changes in N512-N216 (Fig. 2b). Over the Amazon Basin, significant changes are found in both
223 N216-N96 and N512-N216. Over the Amazon Basin and northern Argentina, increasing resolution
224 increases precipitation, which strengthens the N96 wet bias. Over north-eastern Brazil, the significant
225 increase in precipitation with resolution reduces the N96 dry bias. However, the improvement is primarily
226 found in N216-N96; resolutions higher than N216 do not appear to be useful. Over the Ocean, increased
227 resolution is associated with strong changes in precipitation, i.e. precipitation increases over the eastern
228 Pacific Ocean and decreases over the tropical Atlantic Ocean (especially just offshore of most coastal
229 regions) (Fig. 2), but most of the effect comes from moving from N96 to N216.

230
231 Changes in evaporation with resolution are significant over the eastern Pacific Ocean, and over the south-
232 west Atlantic Ocean, along the coast of South America (Fig. 2d-f). However, increasing resolution leads to
233 only moderate changes in evaporation over land. Unlike evaporation, differences in moisture flux
234 convergence (i.e. precipitation minus evaporation) are strong over both land and ocean (Fig. 2g-i).
235 Therefore, the sensitivity of Amazon Basin and Andes precipitation to resolution is mostly due to sensitivity
236 in moisture transport rather than in local moisture recycling (i.e. conversion of local evaporation into
237 precipitation). This is consistent with Vanni re et al. (2019), which showed that ocean-to-land moisture
238 advection increases with resolution. We show small changes in specific humidity and surface air
239 temperature over land (Fig. S1 and Fig. S2). This suggests that changes in precipitation with resolution are
240 due to dynamic changes, rather than thermodynamic changes. Increased resolution is associated with an
241 eastward shift, toward the coast, of the south-east Pacific anticyclonic circulation (Fig. 2g-i) in the southern



242 Pacific coastal region. The wind speed then strengthens and increases evaporation (Fig. 2d-f) and decreases
243 moisture convergence (Fig. 2g-i). Over land, changes in wind speed are particularly strong over the
244 mountains.

245 **3.2 Seasonal means**

246 We next examine the influence of resolution on seasonal rainfall, motivated by the strong seasonal cycle of
247 South American rainfall (i.e., heavy rainfall over northern South America in July-September, while the
248 Amazon basin is wetter in DJF than in JAS). Over north-east Brazil, the resolution sensitivity is strongest
249 in DJF and MAM, mainly due N216-N96 (Fig. 3a; Fig. 3c; Fig. 3d and Fig. 3f), while the N512-N216
250 differences are moderate (Fig. 3b and Fig. 3e). Differences are also strong over the Amazon Basin, in DJF
251 and SON, where increased resolution increases mean precipitation (Fig. 3c and Fig. 3l). Changes in Amazon
252 Basin precipitation are contributed by both N216-N96 (Fig. 3a and Fig. 3j) and N512-N216 (Fig. 3b and
253 Fig. 3k).

254 Over south-western Brazil—northern Argentina, increasing resolution increases precipitation in all seasons
255 which increases the wet bias. These changes are only due to N216-N96 (Fig. 3). Strong differences are also
256 obtained over the tropical Pacific and Atlantic Ocean, from March to November (Fig. 3d, Fig. 3g and Fig.
257 3j), mainly due to N216-N96. N512-N216 does not strongly affect oceanic precipitation (Fig. 3e, Fig. 3h
258 and Fig. 3k).

259 Improvements are shown over north-east Brazil in DJF and MAM. There is little sensitivity to resolution
260 elsewhere in South America. Over the Amazon, changes are stronger in austral summer (i.e. DJF), during
261 the monsoon, but biases are higher at high resolution.

262
263
264
265
266
267
268
269



270

271

272 **4. Seasonal to interannual variability and teleconnections**

273 We have shown a limited effect of resolution on mean precipitation. However, climate variability could be
274 more sensitive to resolution because resolution may affect how the model simulates precipitation
275 distribution, local and large-scale atmospheric dynamics, land-atmosphere coupling and mesoscale
276 systems. Assessing climate variability provides useful information on the ability of climate models to
277 simulate the climate system.

278 The pattern in annual precipitation variance follows the pattern in annual mean precipitation, i.e. higher
279 along the equator than over the surrounding regions (Fig. 4a). At all resolutions, HadGEM3 overestimates
280 precipitation variability over south-east Brazil, and underestimates precipitation variability between 15°S
281 and the equator (Fig. 4b-d). HadGEM3 overestimates both mean precipitation and precipitation variability
282 over parts of the Andes and south-east Brazil/northern Argentina (Fig. 1b-d and Fig. 4b-d). HadGEM3 has
283 a mean wet bias but underestimates the precipitation variability over the Amazon Basin, although increasing
284 resolution reduces the variability bias (Fig 4.e-g). Over south-east Brazil, increasing resolution slightly
285 reduces the overestimation of precipitation variance (Fig. 4e-g). There are no changes in precipitation
286 variance over north-east Brazil, in N512-N96 (Fig. 4e, Fig. 4f and Fig. 4g).

287 Precipitation variance also increases with resolution for individual seasons (not shown). Because both
288 Pacific and Atlantic SSTs affect seasonal-to-interannual South American precipitation variability, we
289 hypothesized that changes in variance to be associated with a change in the strength of the teleconnection
290 between ENSO and South American precipitation, and between the South Atlantic SSTs and South
291 American precipitation. However, this hypothesis was not supported by the following evidences: The
292 impact of ENSO on South America is assessed through regressing the El Niño 3.4 index (170-120°W; 5°S-
293 5°N) onto precipitation for each grid point, focusing on the seasonal anomalies (Fig. S3). We found that
294 increasing horizontal resolution does not systematically alter the influence of ENSO on Brazilian



295 precipitation. These analyses were repeated, focusing on tropical Atlantic gradients in SST, yielding a
296 similar conclusion to the one for ENSO, i.e. increasing the horizontal resolution does not change impacts
297 of the SST on precipitation over land (not shown).

298



299 **5. Daily to sub-seasonal variability and teleconnections**

300 **5.1 Daily variability**

301 Daily precipitation variance is more sensitive to resolution than monthly or annual variance. Over the
302 Amazon Basin, differences between the simulations are stronger in austral summer than other seasons (Fig.
303 S4). Besides, precipitation variability is strongly tied to the South American summer monsoon, which
304 mainly occurs in DJF. Therefore, we focus further analysis on daily variance and on DJF.

305 In DJF, N96 underestimates daily precipitation variance (Fig. 5a). N216 and N512 outperform N96, with a
306 reduced underestimation of precipitation variance over the Amazon Basin (Fig. 5b and Fig. 5c). The
307 increase in variance is due to shifts from N96 to N216 and N216 to N512 (Fig. 5d and Fig. 5e). The
308 difference in P-E variance is high, close to the difference in P variance (Fig. 5g; Fig. 5h and Fig. 5i).
309 Therefore, changes in precipitation variance are mostly associated with changes in the variance of moisture
310 flux convergence.

311 Biases in DJF daily precipitation variance have also been assessed using CMORPH over 1998-2014. The
312 same conclusions are drawn: N96 underestimates variance and N512 overestimates variance (Fig. S4).
313 However, the N96 biases are much reduced when compared to CMORPH instead of GPCC, such that N96
314 outperforms N216 and N512 (Fig. S4 and Fig. S5). In addition, the northern Brazil circulation is dominated
315 by easterlies (Fig. 1a), whose variability reinforces by increasing the horizontal resolution (Fig. S6). Over
316 southern Brazil, the circulation is dominated by northerlies; increasing resolution increases meridional wind
317 variance (Fig. S7). Therefore, we suggest the change in precipitation variance is associated with changes in
318 atmospheric dynamics. A positive feedback exists since an increase in precipitation is associated with a
319 strengthening of local vertical velocity, which strengthens the low-level wind. However, changes in wind
320 variance exhibit a large-scale pattern that suggests changes that are not due solely to local precipitation
321 increases. The variance of the meridional wind increases strongly over the eastern side of the Andes (Fig.
322 S7), highlighting the importance of the orography in modulating the circulation and transporting moisture.



323 We analyzed the variance of the zonal and meridional components of the moisture flux and found the same
324 patterns as for the low-level wind (not shown), suggesting that changes are mostly attributed to dynamic
325 changes, rather than thermodynamic changes.

326 **5.2 Effects of the Madden-Julian Oscillation**

327 The Madden Julian Oscillation (MJO) strongly affects sub-seasonal precipitation variability over Brazil
328 (Grimm and Silva Dias 1995; Marengo et al. 2008, 2011, 2013; Grimm and Tedeschi 2009; Lewis et al.
329 2011; Grimm 2019). Therefore, a change in the MJO teleconnection to South America may alter
330 precipitation mean and variance.

331 Indices of the Madden-Julian Oscillation (MJO) have been computed using NCEP for observed wind and
332 outgoing longwave radiation from NOAA Cooperative Institute for Research in Environmental Sciences
333 data set (Liebmann and Smith 1996), following Wheeler and Hendon (2004), by computing empirical
334 orthogonal functions on daily values of 850 and 200 hPa zonal winds and outgoing longwave radiation.
335 Simulated MJO indices are performed by projecting model data onto the reanalysis EOFs, after first
336 removing the model annual mean and the first three harmonics of the model annual cycle. MJO indices
337 were computed on data first interpolated on a 2.5° resolution. See Wheeler and Hendon (2004) for a longer
338 description of the method. Time series have been deseasonalised and linearly detrended prior to computing
339 impacts of MJO on precipitation mean and variance.

340 In observations (GPCC), the MJO strongly impacts tropical South American precipitation, leading to above
341 average precipitation during phases 1 and 8, while phases 3, 4 and 5 are associated with anomalously dry
342 conditions (Fig. 6, top two rows), as shown in Grimm (2019). South of 20°S, phases 1, 2 7 and 8 are
343 associated with anomalously dry conditions and phases 3, 4 and 5 with anomalously wet conditions (Fig.
344 6, top panel). We select two areas, the Amazon Basin, where differences in precipitation variance between
345 simulations are strong and East Brazil, which is strongly impacted by the MJO. Note the boxes on Fig. 6a.



346 Both areas experience above average precipitation during MJO phases 1, 7 and 8, and below average
347 precipitation during phases 3, 4 and 5 (Fig. 6a-b). HadGEM3 reproduces the impact of MJO on East Brazil
348 and Amazon Basin precipitation in sign and magnitude (Fig. 6i-j). There are no clear differences between
349 N96, N216 and N512 simulations, and an impact of the horizontal resolution does not emerge.

350 We show strong impacts of resolution on precipitation variance in Sect. 5.1. Therefore, we address here
351 how precipitation variance could be affected by resolution within each MJO phase. Results are given
352 relative to the variance of the precipitation computed from the full original daily timeseries (with no
353 selection of any specific MJO phases). Results for precipitation variance differ slightly from those for the
354 mean precipitation, with for instance a decrease in the variance during phase 1 when mean precipitation is
355 higher, and stronger during phase 3 when mean precipitation is lower. This difference could also arise from
356 local differences that could strongly impact the area-average. HadGEM3 simulates well the impact of the
357 MJO on the precipitation variance, with above average variance during phases 7 and 8 and below average
358 variance during phases 4 and 5. Unlike the observation, HadGEM3 simulates an increase in the variance of
359 the precipitation during phase 1 of the MJO. N216 and N512 simulations perform better than N96 for phase
360 3 of the MJO, since the N96 simulates reduced precipitation variance while the variance is anomalously
361 high in observation and in the N512 and N216 simulations. However, there is no clear sensitivity of MJO-
362 related precipitation variance to horizontal resolution.

363

364 **5.3 Land-atmosphere feedback**

365 Soil moisture memory contributes to atmospheric variability and could potentially affect the development
366 of the South American Monsoon System. Land-atmosphere coupling is particularly strong over South
367 America (Koster et al. 2004; Sörensson and Menéndez 2011). In this section we assess the sensitivity of
368 land-atmosphere feedbacks to resolution, using ERA-interim as verifying “observations”. The coupling



369 strength metric is defined as the correlation between two variables, weighted by the standard deviation of
370 the reference variable (see Sect. 2.4).

371 Over the Amazon Basin, there is a positive relationship between observed precipitation and observed soil
372 moisture (Fig. 7a), such that an increase in precipitation is associated with anomalously high soil moisture,
373 with soil moisture are coincident with changes in precipitation (Fig. 7e). Over the Amazon Basin and in all
374 HadGEM3 resolutions, the bias in the precipitation—soil moisture coupling strength is small (Fig. 7b-d)
375 and increase in the resolution does not change precipitation—soil moisture coupling strength (Fig. 7i-k;
376 Fig. 7l-n), probably because, over the Amazon, the soil is saturated, such that increases in precipitation
377 variability do not impact soil moisture variability. Soil moisture and evaporation are negatively correlated
378 in observations, such that increased evaporation decreases soil moisture, over the Amazon Basin (Fig. 8a).
379 Over the Amazon Basin, there is not a strong lead-lag relationship between soil moisture and evaporation
380 in observations (Fig. 8e) or in HadGEM3 (Fig. 8f-h). The coupling strength is overestimated in N96 (Fig.
381 8b) but an increase in resolution reduces this overestimation (Fig. 8c-d and Fig.8f-g). Over the Amazon
382 Basin, the moisture budget is energy-limited, rather than moisture limited (Cook et al. 2014). Therefore,
383 we also assessed the coupling strength between temperature and evaporation. An increase in temperature is
384 associated with increased evaporation (Fig. S8) and thus decreased soil moisture, but, in HadGEM3, this
385 coupling strength is not sensitive to resolution (Fig. S8). These results are consistent with our previous
386 results, showing that local recycling plays a moderate role in explaining changes in precipitation variance,
387 which is mainly associated with change in the moisture convergence variability (Fig. 6), rather than with a
388 stronger land-atmosphere coupling (Fig. 8).

389 Outside of the Amazon Basin, the soil moisture-precipitation relationship is positive in both observations
390 (Fig. 7a) and HadGEM3 (Fig. 7b-d), with precipitation variability leading soil moisture variability (Fig. 7b
391 and Fig. 7f-h). The increase in soil moisture increases evaporation over eastern Brazil (Fig. 8a). The soil
392 moisture—evaporation coupling strength is too high in all simulations over north-eastern and eastern Brazil
393 (Fig. 8b-d), with soil moisture driving evaporation, because evaporation is moisture-limited over north-east



394 Brazil, with changes in evaporation leading changes in temperature (Fig. S8). The strengths of both
395 precipitation—soil moisture and soil moisture—evaporation couplings are overestimated in N96 (Fig. 7b
396 and Fig.8b) over eastern Brazil. Increasing resolution reduces this overestimation (Fig. 7cd; Fig. 7i-k; Fig.
397 8cd; Fig, 8i-k).

398
399
400

401 **5.4 Scales of precipitation**

402

403 We use the ASoP diagnostics (see section 2.4) to assess daily precipitation features over South America in
404 HadGEM3, and verify them against CMORPH. We compute the fractional contribution to total CMORPH
405 precipitation from four precipitation intensity bins, over South America, with a focus over two sub-regions,
406 the Amazon Basin (AMZ) and southeast South America (SESA). We compare spatial and temporal scales
407 of precipitation features across datasets for the two subregions. Results are given, separately, for light,
408 moderate and heavy rainfall events. We focus on the occurrence and duration of dry spells.

409

410

411 **5.4.1 Light precipitation and dry spells**

412 In CMORPH, light precipitation events ($<10 \text{ mm.day}^{-1}$) contribute the most of all intensity categories to
413 total precipitation over most of the Andes and northern and southern South America, the Pacific Ocean and
414 western Atlantic Ocean (Fig. 9a). N96 underestimates contributions from light precipitation events over the
415 Andes and south-east Brazil, but overestimates contributions from light precipitation over the Amazon
416 Basin and eastern Brazil (Fig. 9e). The results are consistent with Seth et al. (2004), which also show an
417 overestimation of the percentage of light rain events over South America. This bias is reduced by increasing
418 resolution to N216 and N512 (Fig. 9i-p; Fig. S9).

419 Figure 10 shows frequencies of precipitation events, as classified by intensity and duration. Results are
420 shown for two regions: AMZ, where variance is too weak; and SESA, where variance is too high. Over



421 AMZ and SESA, near-zero precipitation (rainy events of $0.1 - 1 \text{ mm.day}^{-1}$) can last for more than 15 days,
422 while events of $1 - 10 \text{ mm.day}^{-1}$ can last for up to 4 or 5 days (Fig. 10a and Fig. 10f). Over AMZ, N96
423 overestimates the frequency of events of 2 to 12 mm.day^{-1} and underestimates the frequency of those of less
424 than 1 mm.day^{-1} , compared to CMORPH (Fig. 10b). For SESA, N96 underestimates the frequency of
425 precipitation events of less than 1 mm.day^{-1} and lasting between 1 and 8 days; the model overestimates the
426 frequency of near-zero rainy days, lasting more than 8 days (Fig. 10g). Intensity-duration biases improve
427 with resolution over AMZ (Fig. 10c-10d) and SESA (Fig. 10h-10i). However, the biases worsen with
428 resolution for near-zero precipitation lasting for any duration over AMZ, and for intensities between 1-9
429 mm.day^{-1} with a duration of 1-5 days over SESA.

430 In addition to events of less than 10 mm.day^{-1} , we assess simulated frequency and duration of dry spells,
431 defined by events of less than 0.1 mm.day^{-1} . We create 2-D histograms for duration versus frequency of dry
432 days over AMZ and SESA (Fig. 11). CMORPH shows more frequent short-duration dry spells as compared
433 to HadGEM3 over AMZ at both native (Fig. 11a) and N96 (Fig. 11c) resolutions. Over SESA, CMORPH
434 also generally shows more frequent dry spells for durations longer than 1 day (Fig. 11b, 11d). The sensitivity
435 of dry-spell frequency to model resolution is generally smaller than the model bias. Once all datasets are
436 interpolated to the common N96 resolution, N96 produces longer and more frequent dry spells than N216
437 and N512, and is closer to CMORPH.

438 **5.4.2 Moderate precipitation**

439 Over most other parts of South America (i.e. Amazon and central and eastern Brazil), most of the total
440 precipitation is contributed by light to moderate events ($10-40 \text{ mm.day}^{-1}$; Fig. 9a-c). Compared to
441 CMORPH, N96 overestimates the contribution from moderate events, to total precipitation, over the Andes
442 and underestimates this contribution over South America outside of the Andes (Fig. 9f, 9g). Although the
443 spatial pattern of biases is similar to N96, biases in contribution from moderate rainfall to total precipitation
444 reduce when increasing resolution (Fig. 9f-j-n and Fig. 9g-k-o; Fig. S9).



445 Over AMZ and SESA, most precipitation comes from moderate events in both CMORPH and HadGEM3
446 (Fig. 10b-e). Over AMZ, CMORPH distribution peaks at $\sim 30 \text{ mm.day}^{-1}$ (Fig. 10b, 10d), when using the
447 CMORPH native grid (Fig. 10b), and at $\sim 20 \text{ mm.day}^{-1}$ when using the N96 grid (Fig. 10d). At their native
448 resolutions, N96, N216 and N512 have a primary peak at $\sim 9 \text{ mm.day}^{-1}$ and a secondary peak at $\sim 30 \text{ mm.day}^{-1}$
449 ¹ (Fig. 10b). On the N96 grid, the secondary peak is removed in N216 and N512. As the fractional
450 contribution in HadGEM3 peaks at lower intensities for all three resolutions, HadGEM3 overestimates the
451 contribution from intensities below $\sim 15 \text{ mm.day}^{-1}$ and underestimates contribution from intensities above
452 15 mm.day^{-1} (Fig. 10b). When compared on their native grids, the model biases reduce with resolution over
453 AMZ. However, once interpolated to N96, N512 has the largest bias in fractional contribution, around the
454 peak intensity (i.e. at $\sim 10 \text{ mm.day}^{-1}$). Over AMZ, N96 underestimates the frequency of events of 12-40
455 mm.day^{-1} (Fig. 10d and Fig. 12b). Increasing resolution reduces the biases for the frequency of events of
456 12-25 mm.day^{-1} but leads to an underestimation of precipitation of 30 to 40 mm.day^{-1} (Fig. 10b and Fig.
457 12c-e). Over SESA, distribution peaks at $\sim 20\text{-}30 \text{ mm.day}^{-1}$ (Fig. 10c and Fig. 10e). Over SESA, N96
458 underestimates (overestimates) the frequency of events of 2-20 mm.day^{-1} (20-40 mm.day^{-1}) (Fig. 10e; Fig.
459 12g). These biases are reduced in at N216 and N512 (Fig. 10e; Fig. 12h-j).

460 **5.4.3 Heavy precipitation**

461 Parts of the Peruvian Andes, Uruguay and eastern Argentina receive most of their rainfall from heavy events
462 ($>40 \text{ mm.day}^{-1}$; Fig. 9d). N96 overestimates these contributions ($>40 \text{ mm.day}^{-1}$) over central Brazil, the
463 eastern Amazon and south-eastern Brazil (Fig. 9h). Like for the light and moderate events, increasing
464 resolution reduces these biases (Fig. 9h-p and Fig. S9). This suggests that, at higher resolution, HadGEM3
465 performs better for the frequency of extreme events, such as those that lead to flooding. However, the
466 improvements primarily come from the increase from N96 to N216, not from N216 to N512 (Fig. S9). In
467 addition, N96 overestimates the frequency of events $> 40 \text{ mm.day}^{-1}$ over AMZ and SESA (Fig. 10b; Fig.
468 10g). Increasing resolution reduces these biases, again mostly due to increase from the N96 to N216



469 resolution, not from N216 to N512. For AMZ, N512 has a higher bias than N216 for events of 40-90
470 mm.day⁻¹.

471

472 **5.4.4 Temporal and spatial scales**

473

474 To compare spatial and temporal scales of precipitation features across datasets, we plot correlations as
475 functions of time (Fig. 13a-d) and distance (Fig. 13e-h) (see section 2.4). Over AMZ, N96 overestimates
476 the spatial and temporal scales of precipitation events relative to CMORPH, on their native grids (Fig. 13a
477 and Fig. 13e). However, once CMORPH is interpolated to the N96 grid, N96 simulation underestimates the
478 spatial scale (and overestimates the temporal scale) of precipitation (Fig 13b and Fig. 13f), highlighting that
479 results strongly depend on the analysis grid. For SESA, N96 also underestimates the spatial scale and
480 overestimates temporal scale of precipitation (Fig. 13d-g-h). When considering native grids only, there are
481 no clear differences between N96 and CMORPH for the spatial extent of precipitation events (Fig. 13c).

482 On native grids, N96 simulates events with larger spatial scales than N216 and N512 (Fig. 13a). However,
483 this is mainly due to the coarse N96 grid. While all datasets are interpolated onto the N96 grid, N96 events
484 are smaller than those in N216 and N512, which show similar scales and are closer to CMORPH (Fig. 13b).
485 Over SESA, spatial scales are similar in all simulations, on their native grids (Fig. 13c). However, as for
486 AMZ, at N96 resolution N512 and N216 are closer to CMORPH than to N96 (Fig. 13d). For both AMZ
487 and SESA, therefore, the spatial features of daily precipitation events are better simulated at higher
488 resolution.

489 At all resolutions, precipitation features persist longer than in CMORPH (Fig. 13e-h). Over AMZ and
490 SESA, biases are lowest in N96, which simulates events that are less persistent than in N216 and N512
491 (Fig. 13f, Fig. 13h). This bias increases at higher resolution. Therefore, increasing horizontal resolution
492 does not improve biases in temporal scales of precipitation.



493 **6 Conclusion**

494

495

496 We assess the effects of increasing horizontal resolution on simulated South American precipitation. We
497 use atmosphere-only simulations, performed with HadGEM3-GC3.1 (Williams et al. 2018) at three
498 horizontal resolutions: N96 (~130 km, $1.88^\circ \times 1.25^\circ$), N216 (~60 km, $0.83^\circ \times 0.56^\circ$), and N512 (~25 km,
499 $0.35^\circ \times 0.23^\circ$). We assess, systematically, how the step change between each resolution effects simulated
500 precipitation, focusing on precipitation mean and variance, and on fine scale processes, such as temporal
501 and spatial scales, frequency of heavy and light precipitation events and dry-spell durations.

502

503 We show that the atmosphere-only simulations have systematic biases in simulating annual mean and
504 seasonal mean precipitation over South America. North-east Brazil is anomalously dry, while the southeast
505 Brazil and the Andes are too wet. These biases are mostly due to atmospheric circulation biases:
506 underestimated trade easterlies, and a displaced anticyclonic circulation over southeast Brazil, both acting
507 to modify moisture transport over South America. Increasing horizontal resolution affects the simulated
508 precipitation. For instance, precipitation biases reduce over the Andes and over northeast Brazil. It is worth
509 increasing the resolution to N512 (~25 km) for simulating precipitation over the Andes Mountains. This is
510 consistent with Vanni re et al. (2019), which shows that the added value of increasing horizontal resolution
511 is greatest over orography. Over northeast Brazil, the largest improvement comes from increasing resolution
512 to N216 (~60 km); a further increase to N512 is only associated with moderate changes. Increasing
513 resolution does not improve model biases over the Amazon Basin. These results are consistent with Roberts
514 et al. (2018) for the Amazon Basin and northeast and south Brazil. In addition, improvements vary
515 seasonally: changes are the strongest over northeast Brazil in DJF and MAM, when precipitation is also
516 highest. Over the Andes, the results are similar in all seasons.

517

518 Biases in mean precipitation are collocated with biases in regional precipitation variance. For instance,
519 northeast Brazil is too dry and HadGEM3-GC3.1 systematically underestimates precipitation variance,



520 while southeast Brazil is too wet and HadGEM3-GC3.1 systematically overestimates precipitation
521 variance. However, this does not hold for the Amazon Basin, which is too wet but where the precipitation
522 variance is strongly underestimated. Precipitation variance is stronger at daily scales than at monthly scales;
523 biases are strongest in DJF and over the Amazon Basin. Increasing resolution increases precipitation
524 variance, hence reducing biases. The increase in precipitation variance is associated with an increase in
525 moisture flux convergence variance over land, and with changes in the variance of the low-level winds;
526 local recycling of evaporation has a limited role. Relatedly, coupling strengths between evaporation, soil
527 moisture and precipitation are only weakly sensitive to resolution, except for some improvements in
528 coupling strength over eastern and south-eastern Brazil. We found only modest sensitivity to resolution for
529 the teleconnections of the El-Niño Southern Oscillation and Madden-Julian Oscillation to land
530 precipitation. This suggests that changes in precipitation mean and variance are not due to changes in these
531 teleconnections.

532
533 HadGEM3-GC3.1 has biases in its precipitation distribution. For instance, the model does not produce
534 enough dry days over the Amazon Basin or moderate rain days ($10-40 \text{ mm.day}^{-1}$), while simulating too
535 many light events ($<10 \text{ mm.day}^{-1}$) and heavy events ($>40 \text{ mm.day}^{-1}$). Over south-east Brazil, the model
536 simulates too few short dry spells and too many long ones. HadGEM3-GC3.1 simulates too few and too
537 short events of 2 to 16 mm.day^{-1} , but simulates too many and too long events of more than 20 mm.day^{-1} .
538 These metrics are important for understanding the ability of climate models to simulate high-impact events.
539 Increasing resolution reduces these biases; N512 is therefore better at simulating precipitation distributions
540 than N96. In addition, increasing the horizontal resolution increases the spatial scale of daily rain events,
541 suggesting a better simulation of organised mesoscale systems. However, the persistence of precipitation
542 events is better simulated at N96, showing no clear sensitivity to resolution. Other models also overestimate
543 light events at the expense of heavy events over the Amazon and eastern Brazil, and overestimate heavy
544 events at the expense of lighter ones in southeast Brazil (Seth et al. 2004).

545



546 Over South America, precipitation results from the combination of the predominant role played by the
547 InterTropical Convergence Zone and the South Atlantic Convergence Zone (Waliser et al. 1993; Liebmann
548 et al. 1999). In addition, mesoscale systems such as squall lines may be responsible for a large fraction of
549 Amazonian precipitation (Cohen et al. 1995). Our results show that increasing the horizontal resolution
550 increases the spatial scale of rain events, i.e. of the mesoscale systems, over both Amazonia and south-east
551 Brazil. Therefore, we speculate that increasing resolution could lead to more organized convective systems,
552 which would be consistent with the increase in moisture flux convergence, as shown over South America
553 at the highest resolution. This would be consistent with Vellinga et al. (2016) who showed that N512
554 resolution improved mesoscale systems over West Africa relative to N96 or N216. Conversely, the decrease
555 in the persistence of such events (highest at the N96 resolution) could be associated with an increase in
556 daily rainfall variability, because of less persistent rainy events. Those are hypotheses that should be
557 assessed in more detail in a specific study, potentially with models at sufficiently high resolution to disable
558 convective parameterisations.

559

560 The mechanism for increases in precipitation variance with resolution are still unclear. The increase in
561 precipitation variance is a global feature, not limited to South America (Fig. S10). Further work is needed
562 to understand better this behavior at global scale. Besides, we used AMIP-type simulations; and results
563 could be different in coupled models, in which the ocean can interact with atmospheric variability,
564 particularly when accounting for SST teleconnections.

565

566

567

568

569

570

571



572 **Code availability.** Codes used to perform analysis and figures are publicly available at
573 <https://doi.org/10.5281/zenodo.3840095>. For the analysis of the scales of precipitation (ASoP), codes are
574 available on <https://github.com/nick-klngaman/dubstep/tree/master/asop> and [https://github.com/nick-](https://github.com/nick-klngaman/dubstep/tree/master/asop_duration)
575 [klngaman/dubstep/tree/master/asop_duration](https://github.com/nick-klngaman/dubstep/tree/master/asop_duration).

576

577 **Data availability.** The model data used in the analysis are available from the CMIP6 Earth System Grid
578 Federation, for N96 (HadGEM3-GC31-LM), N216 (HadGEM3-GC31-MM) and N512 (HadGEM3-
579 GC31-HM). The list of persistent identifiers of the data we have used is available at
580 <https://doi.org/10.5281/zenodo.3840095>

581

582 **Author contributions.** AC, PAM and PC performed the data analysis. PAM prepared the manuscript
583 with contributions from all co-authors.

584

585

586 **Acknowledgements**

587 This work was supported by the Newton Fund through the Met Office Climate Science for Service
588 Partnership Brazil (CSSP Brazil). NPK was funded by an Independent Research Fellowship from the
589 Natural Environment Research Council (NE/L010976/1) and by the NERC/GCRF programme
590 Atmospheric hazard in developing countries: risk assessment and early warnings (ACREW). Detailed
591 calculations and code for the ASoP diagnostics are available at
592 https://github.com/achevuturi/asop_duration. NOAA OLR data can be obtained from the website
593 (https://www.esrl.noaa.gov/psd/data/gridded/data.interp_OLR.html).

594

595



596 **References**

- 597 Bacmeister JT, Wehner MF, Neale RB, et al (2013) Exploratory High-Resolution Climate Simulations
598 using the Community Atmosphere Model (CAM). *J Clim* 27:3073–3099. doi: 10.1175/JCLI-D-13-
599 00387.1
- 600 Bombardi RJ, Carvalho LM V (2008) IPCC global coupled model simulations of the South America
601 monsoon system. *Clim Dyn* 33:893. doi: 10.1007/s00382-008-0488-1
- 602 Coelho CAS, de Oliveira CP, Ambrizzi T, et al (2016) The 2014 southeast Brazil austral summer drought:
603 regional scale mechanisms and teleconnections. *Clim Dyn* 46:3737–3752. doi: 10.1007/s00382-015-
604 2800-1
- 605 Cohen JCP, Silva Dias MAF, Nobre CA (1995) Environmental Conditions Associated with Amazonian
606 Squall Lines: A Case Study. *Mon Weather Rev* 123:3163–3174. doi: 10.1175/1520-
607 0493(1995)123<3163:ECAWAS>2.0.CO;2
- 608 Cook BI, Smerdon JE, Seager R, Coats S (2014) Global warming and 21st century drying. *Clim Dyn*
609 43:2607–2627. doi: 10.1007/s00382-014-2075-y
- 610 Custódio M de S, Porfírio da Rocha R, Vidale PL (2012) Analysis of precipitation climatology simulated
611 by high resolution coupled global models over the South America. *Hydrol Res Lett* 6:92–97. doi:
612 10.3178/hrl.6.92
- 613 Dai A (2006) Precipitation Characteristics in Eighteen Coupled Climate Models. *J Clim* 19:4605–4630.
614 doi: 10.1175/JCLI3884.1
- 615 De Sales F, Xue Y (2011) Assessing the dynamic-downscaling ability over South America using the
616 intensity-scale verification technique. *Int J Climatol* 31:1205–1221. doi: 10.1002/joc.2139
- 617 de Souza Custodio M, da Rocha RP, Ambrizzi T, et al (2017) Impact of increased horizontal resolution in
618 coupled and atmosphere-only models of the HadGEM1 family upon the climate patterns of South
619 America. *Clim Dyn* 48:3341–3364. doi: 10.1007/s00382-016-3271-8
- 620 Dee DP, Uppala SM, Simmons AJ, et al (2011) The ERA-Interim reanalysis: configuration and
621 performance of the data assimilation system. *Q J R Meteorol Soc* 137:553–597. doi: 10.1002/qj.828
- 622 DelSole T, Shukla J (2010) Model Fidelity versus Skill in Seasonal Forecasting. *J Clim* 23:4794–4806.
623 doi: 10.1175/2010JCLI3164.1
- 624 Delworth TL, Rosati A, Anderson W, et al (2011) Simulated Climate and Climate Change in the GFDL
625 CM2.5 High-Resolution Coupled Climate Model. *J Clim* 25:2755–2781. doi: 10.1175/JCLI-D-11-
626 00316.1
- 627 Demory M-E, Vidale PL, Roberts MJ, et al (2014) The role of horizontal resolution in simulating drivers
628 of the global hydrological cycle. *Clim Dyn* 42:2201–2225. doi: 10.1007/s00382-013-1924-4
- 629 Doblus-Reyes FJ, Andreu-Burillo I, Chikamoto Y, et al (2013) Initialized near-term regional climate
630 change prediction. *Nat Commun* 4:1715. doi: 10.1038/ncomms2704
- 631 Falco M, Carril AF, Menéndez CG, et al (2019) Assessment of CORDEX simulations over South



- 632 America: added value on seasonal climatology and resolution considerations. *Clim Dyn* 52:4771–
633 4786. doi: 10.1007/s00382-018-4412-z
- 634 Gent PR, Yeager SG, Neale RB, et al (2010) Improvements in a half degree atmosphere/land version of
635 the CCSM. *Clim Dyn* 34:819–833. doi: 10.1007/s00382-009-0614-8
- 636 Grimm AM (2019) Madden–Julian Oscillation impacts on South American summer monsoon season:
637 precipitation anomalies, extreme events, teleconnections, and role in the MJO cycle. *Clim Dyn*. doi:
638 10.1007/s00382-019-04622-6
- 639 Grimm AM, Silva Dias PL (1995) Analysis of Tropical–Extratropical Interactions with Influence
640 Functions of a Barotropic Model. *J Atmos Sci* 52:3538–3555. doi: 10.1175/1520-
641 0469(1995)052<3538:AOTIWI>2.0.CO;2
- 642 Grimm AM, Tedeschi RG (2009) ENSO and Extreme Rainfall Events in South America. *J Clim* 22:1589–
643 1609. doi: 10.1175/2008JCLI2429.1
- 644 Haarsma RJ, Roberts MJ, Vidale PL, et al (2016) High resolution model intercomparison project
645 (HighResMIP v1. 0) for CMIP6. *Geosci Model Dev* 9:4185–4208
- 646 Jia L, Yang X, Vecchi GA, et al (2014) Improved Seasonal Prediction of Temperature and Precipitation
647 over Land in a High-Resolution GFDL Climate Model. *J Clim* 28:2044–2062. doi: 10.1175/JCLI-D-
648 14-00112.1
- 649 Joyce RJ, Janowiak JE, Arkin PA, Xie P (2004) CMORPH: A Method that Produces Global Precipitation
650 Estimates from Passive Microwave and Infrared Data at High Spatial and Temporal Resolution. *J*
651 *Hydrometeorol* 5:487–503. doi: 10.1175/1525-7541(2004)005<0487:CAMTPG>2.0.CO;2
- 652 Jung T, Miller MJ, Palmer TN, et al (2011) High-Resolution Global Climate Simulations with the
653 ECMWF Model in Project Athena: Experimental Design, Model Climate, and Seasonal Forecast
654 Skill. *J Clim* 25:3155–3172. doi: 10.1175/JCLI-D-11-00265.1
- 655 Kanamitsu M, Ebisuzaki W, Woollen J, et al (2002) NCEP–DOE AMIP-II Reanalysis (R-2). *Bull Am*
656 *Meteorol Soc* 83:1631–1643. doi: 10.1175/BAMS-83-11-1631
- 657 Kirtman BP, Bitz C, Bryan F, et al (2012) Impact of ocean model resolution on CCSM climate
658 simulations. *Clim Dyn* 39:1303–1328. doi: 10.1007/s00382-012-1500-3
- 659 Klingaman NP, Martin GM, Moise A (2017) ASoP (v1.0): a set of methods for analyzing scales of
660 precipitation in general circulation models. *Geosci Model Dev* 10:57–83. doi: 10.5194/gmd-10-57-
661 2017
- 662 Knight JR, Folland CK, Scaife AA (2006) Climate impacts of the Atlantic Multidecadal Oscillation.
663 *Geophys Res Lett* 33:L17706. doi: 10.1029/2006GL026242
- 664 Koster RD, Dirmeyer PA, Guo Z, et al (2004) Regions of Strong Coupling Between Soil Moisture and
665 Precipitation. *Science* (80-) 305:1138 LP – 1140. doi: 10.1126/science.1100217
- 666 Koutroulis AG, Grillakis MG, Tsanis IK, Papadimitriou L (2016) Evaluation of precipitation and
667 temperature simulation performance of the CMIP3 and CMIP5 historical experiments. *Clim Dyn*
668 47:1881–1898. doi: 10.1007/s00382-015-2938-x



- 669 Lewis SL, Brando PM, Phillips OL, et al (2011) The 2010 Amazon Drought. *Science* (80-) 331:554 LP –
670 554. doi: 10.1126/science.1200807
- 671 Liebmann B, Kiladis GN, Marengo J, et al (1999) Submonthly Convective Variability over South
672 America and the South Atlantic Convergence Zone. *J Clim* 12:1877–1891. doi: 10.1175/1520-
673 0442(1999)012<1877:SCVOSA>2.0.CO;2
- 674 Liebmann B, Smith CA (1996) Description of a Complete (Interpolated) Outgoing Longwave Radiation
675 Dataset. *Bull Am Meteorol Soc* 77:1275–1277
- 676 Liu WT, Juárez RIN (2001) ENSO drought onset prediction in northeast Brazil using NDVI. *Int J Remote*
677 *Sens* 22:3483–3501. doi: 10.1080/01431160010006430
- 678 Marengo JA, Alves LM, Soares WR, et al (2013) Two Contrasting Severe Seasonal Extremes in Tropical
679 South America in 2012: Flood in Amazonia and Drought in Northeast Brazil. *J Clim* 26:9137–9154.
680 doi: 10.1175/JCLI-D-12-00642.1
- 681 Marengo JA, Nobre CA, Tomasella J, et al (2008) The Drought of Amazonia in 2005. *J Clim* 21:495–
682 516. doi: 10.1175/2007JCLI1600.1
- 683 Marengo JA, Tomasella J, Alves LM, et al (2011) The drought of 2010 in the context of historical
684 droughts in the Amazon region. *Geophys Res Lett* 38:. doi: doi:10.1029/2011GL047436
- 685 Martin GM, Klingaman NP, Moise AF (2017) Connecting spatial and temporal scales of tropical
686 precipitation in observations and the MetUM-GA6. *Geosci Model Dev* 10:105–126. doi:
687 10.5194/gmd-10-105-2017
- 688 McClean JL, Bader DC, Bryan FO, et al (2011) A prototype two-decade fully-coupled fine-resolution
689 CCSM simulation. *Ocean Model* 39:10–30. doi: https://doi.org/10.1016/j.ocemod.2011.02.011
- 690 Power S, Casey T, Folland C, et al (1999) Inter-decadal modulation of the impact of ENSO on Australia.
691 *Clim Dyn* 15:319–324. doi: 10.1007/s003820050284
- 692 Rayner NA, Brohan P, Parker DE, et al (2006) Improved Analyses of Changes and Uncertainties in Sea
693 Surface Temperature Measured In Situ since the Mid-Nineteenth Century: The HadSST2 Dataset. *J*
694 *Clim* 19:446–469. doi: 10.1175/JCLI3637.1
- 695 Roberts MJ, Baker A, Blockley EW, et al (2019) Description of the resolution hierarchy of the global
696 coupled HadGEM3-GC3.1 model as used in CMIP6 HighResMIP experiments. *Geosci Model Dev*
697 12:4999–5028. doi: 10.5194/gmd-12-4999-2019
- 698 Roberts MJ, Vidale PL, Senior C, et al (2018) The Benefits of Global High Resolution for Climate
699 Simulation: Process Understanding and the Enabling of Stakeholder Decisions at the Regional
700 Scale. *Bull Am Meteorol Soc* 99:2341–2359. doi: 10.1175/BAMS-D-15-00320.1
- 701 Sakamoto TT, Komuro Y, Nishimura T, et al (2012) MIROC4h—a new high-resolution atmosphere-
702 ocean coupled general circulation model. *J Meteorol Soc Japan Ser II* 90:325–359
- 703 Schneider U, Becker A, Finger P, et al (2014) GPCP’s new land surface precipitation climatology based
704 on quality-controlled in situ data and its role in quantifying the global water cycle. *Theor Appl*
705 *Climatol* 115:15–40. doi: 10.1007/s00704-013-0860-x



- 706 Seth A, Rojas M, Liebmann B, Qian J-H (2004) Daily rainfall analysis for South America from a regional
707 climate model and station observations. *Geophys Res Lett* 31:. doi: 10.1029/2003GL019220
- 708 Shaffrey LC, Stevens I, Norton WA, et al (2009) U.K. HiGEM: The New U.K. High-Resolution Global
709 Environment Model—Model Description and Basic Evaluation. *J Clim* 22:1861–1896. doi:
710 10.1175/2008JCLI2508.1
- 711 Sierra JP, Arias PA, Vieira SC (2015) Precipitation over northern South America and its seasonal
712 variability as simulated by the CMIP5 models. *Adv Meteorol* 2015:
- 713 Small RJ, Bacmeister J, Bailey D, et al (2014) A new synoptic scale resolving global climate simulation
714 using the Community Earth System Model. *J Adv Model Earth Syst* 6:1065–1094. doi:
715 doi:10.1002/2014MS000363
- 716 Solman SA, Blázquez J (2019) Multiscale precipitation variability over South America: Analysis of the
717 added value of CORDEX RCM simulations. *Clim Dyn* 53:1547–1565. doi: 10.1007/s00382-019-
718 04689-1
- 719 Sörensson AA, Menéndez CG (2011) Summer soil—precipitation coupling in South America. *Tellus A*
720 *Dyn Meteorol Oceanogr* 63:56–68. doi: 10.1111/j.1600-0870.2010.00468.x
- 721 Sun Y, Solomon S, Dai A, Portmann RW (2006) How Often Does It Rain? *J Clim* 19:916–934. doi:
722 10.1175/JCLI3672.1
- 723 Trenberth KE (2011) Changes in precipitation with climate change. *Clim Res* 47:123–138
- 724 Vannière B, Demory M-E, Vidale PL, et al (2019) Multi-model evaluation of the sensitivity of the global
725 energy budget and hydrological cycle to resolution. *Clim Dyn* 52:6817–6846. doi: 10.1007/s00382-
726 018-4547-y
- 727 Vellinga M, Roberts M, Vidale PL, et al (2016) Sahel decadal rainfall variability and the role of model
728 horizontal resolution. *Geophys Res Lett* 43:326–333. doi: 10.1002/2015GL066690
- 729 Villamayor J, Ambrizzi T, Mohino E (2018) Influence of decadal sea surface temperature variability on
730 northern Brazil rainfall in CMIP5 simulations. *Clim Dyn* 51:563–579. doi: 10.1007/s00382-017-
731 3941-1
- 732 Waliser DE, Graham NE, Gautier C (1993) Comparison of the Highly Reflective Cloud and Outgoing
733 Longwave Radiation Datasets for Use in Estimating Tropical Deep Convection. *J Clim* 6:331–353.
734 doi: 10.1175/1520-0442(1993)006<0331:COTHRC>2.0.CO;2
- 735 Walters D, Baran AJ, Boutle I, et al (2019) The Met Office Unified Model Global Atmosphere 7.0/7.1
736 and JULES Global Land 7.0 configurations. *Geosci Model Dev* 12:1909–1963. doi: 10.5194/gmd-
737 12-1909-2019
- 738 Wei J, Dirmeyer PA (2012) Dissecting soil moisture-precipitation coupling. *Geophys Res Lett* 39:. doi:
739 10.1029/2012GL053038
- 740 Wheeler MC, Hendon HH (2004) An All-Season Real-Time Multivariate MJO Index: Development of an
741 Index for Monitoring and Prediction. *Mon Weather Rev* 132:1917–1932. doi: 10.1175/1520-
742 0493(2004)132<1917:AARMMI>2.0.CO;2



743 Williams KD, Copsey D, Blockley EW, et al (2018) The Met Office Global Coupled Model 3.0 and 3.1
744 (GC3.0 and GC3.1) Configurations. *J Adv Model Earth Syst* 10:357–380. doi:
745 doi:10.1002/2017MS001115

746 Willmott CJ, Matsuura K, Legates DR (2001) Terrestrial air temperature and precipitation: monthly and
747 annual time series (1950–1999). *Cent Clim Res version 1*:

748 Yin L, Fu R, Shevliakova E, Dickinson RE (2013) How well can CMIP5 simulate precipitation and its
749 controlling processes over tropical South America? *Clim Dyn* 41:3127–3143. doi: 10.1007/s00382-
750 012-1582-y

751 Zeng N, Yoon J-H, Marengo JA, et al (2008) Causes and impacts of the 2005 Amazon drought. *Environ*
752 *Res Lett* 3:14002. doi: 10.1088/1748-9326/3/1/014002

753

754

755

756

757

758

759

760

761

762

763

764

765

766

767

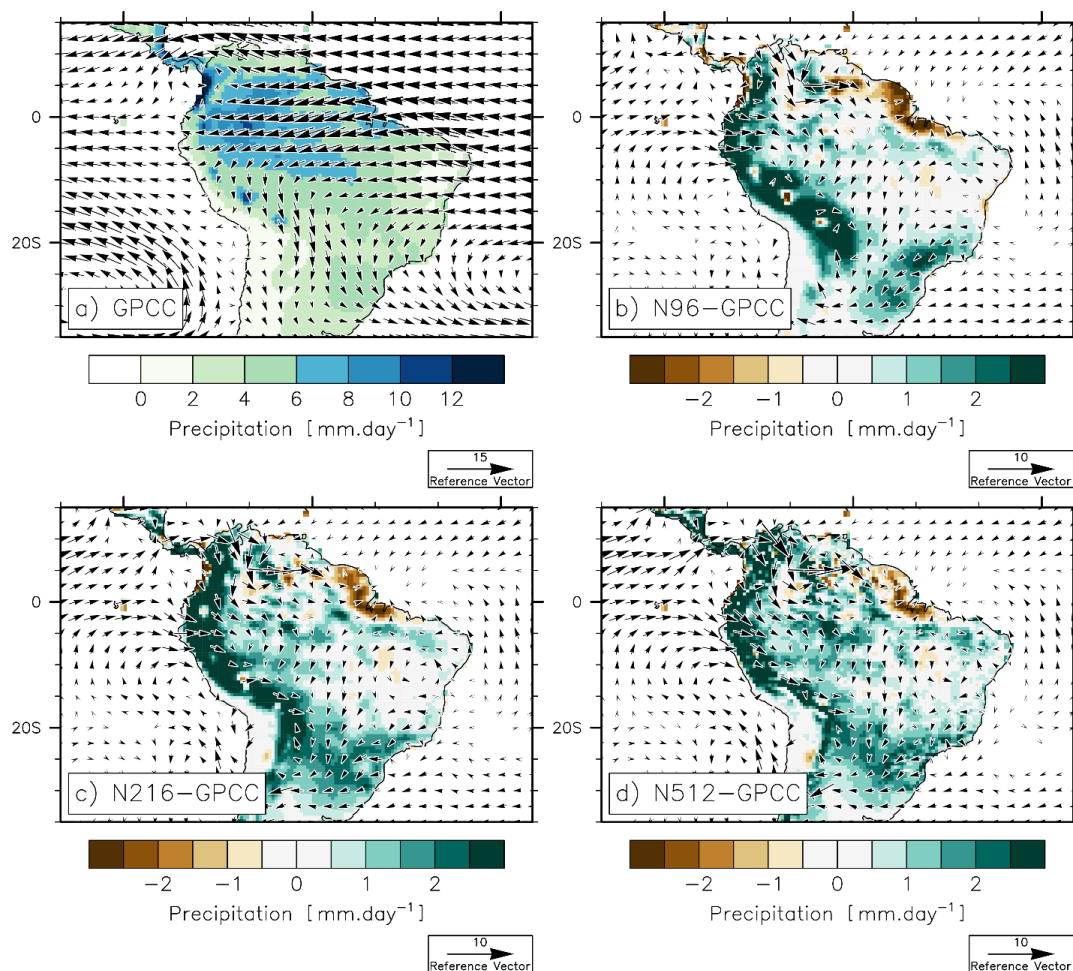
768

769

770



771 **Figures**



772

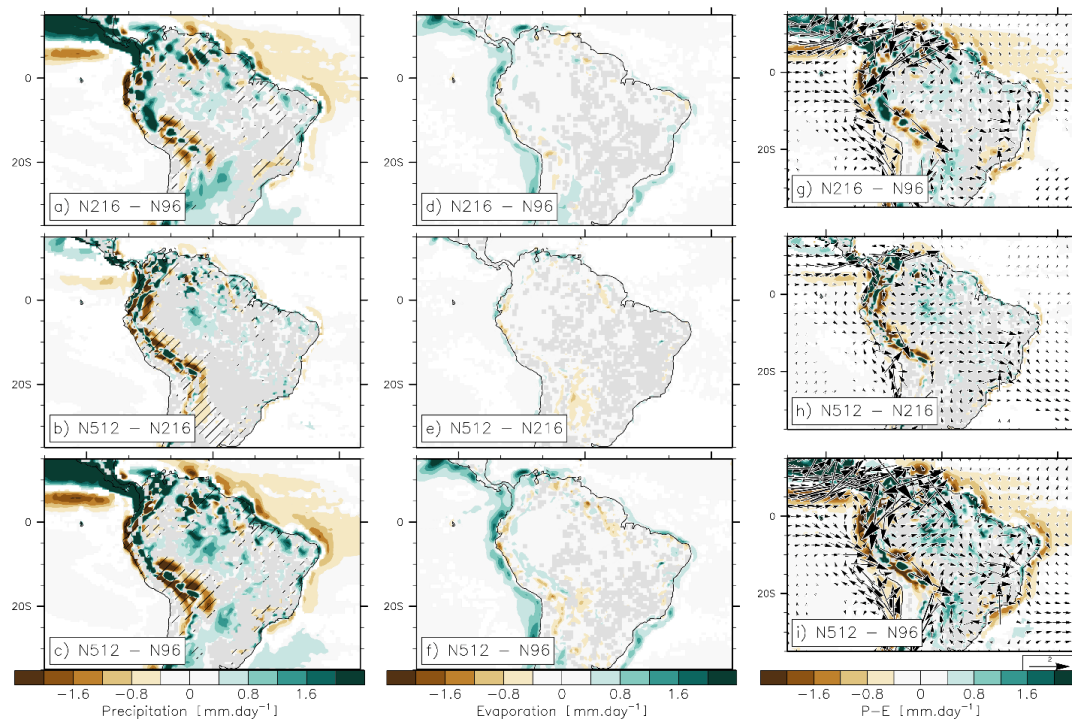
773 **Figure 1:** (a) Observed mean annual precipitation (GPCC; mm.day^{-1} ; colors) and 850 hPa wind (NCEP;
774 m.s^{-1} ; vectors), averaged over the period 1950-2014. Bias in precipitation and 850 hPa wind in (b) N96 (i.e.
775 N96-GPCC), (c) N216 (i.e. N216-GPCC) and (d) N512 (i.e. N512-GPCC). On the panels (a), (b) and (c)
776 biases in precipitation are shown when statistically significant in all of the three members, according to a
777 Student's t-test and a 95% confidence level.

778

779

780

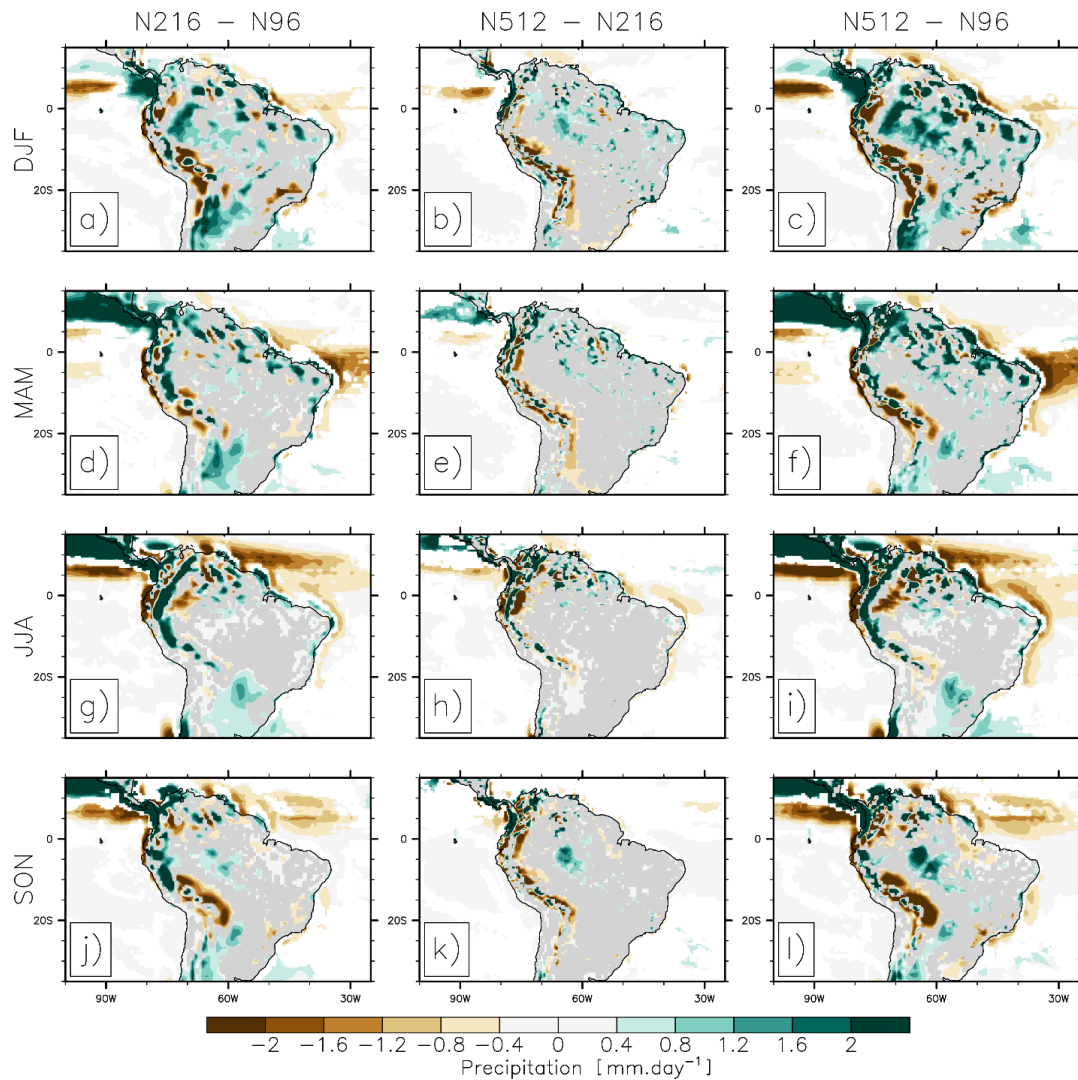
781



782

783 **Figure 2:** Ensemble-mean (a) N216-N96, (b) N512-N216 and (c) N512-N96 differences in mean annual
784 precipitation ($\text{mm}\cdot\text{day}^{-1}$). (d), (e) and (f): same as (a), (b) and (c) but for evaporation ($\text{mm}\cdot\text{day}^{-1}$). (g), (h)
785 and (i): same as (a), (b) and (c) but for the moisture flux convergence (P-E; $\text{mm}\cdot\text{day}^{-1}$; colors) and the 850
786 hPa wind ($\text{m}\cdot\text{s}^{-1}$; vectors). For precipitation (i.e. left row) stippling indicates that the mean bias is reduced
787 at the higher than at the lower horizontal resolution. Differences are shown when significantly different to
788 zero according to a Student's t-test and a 95% confidence level.

789



790

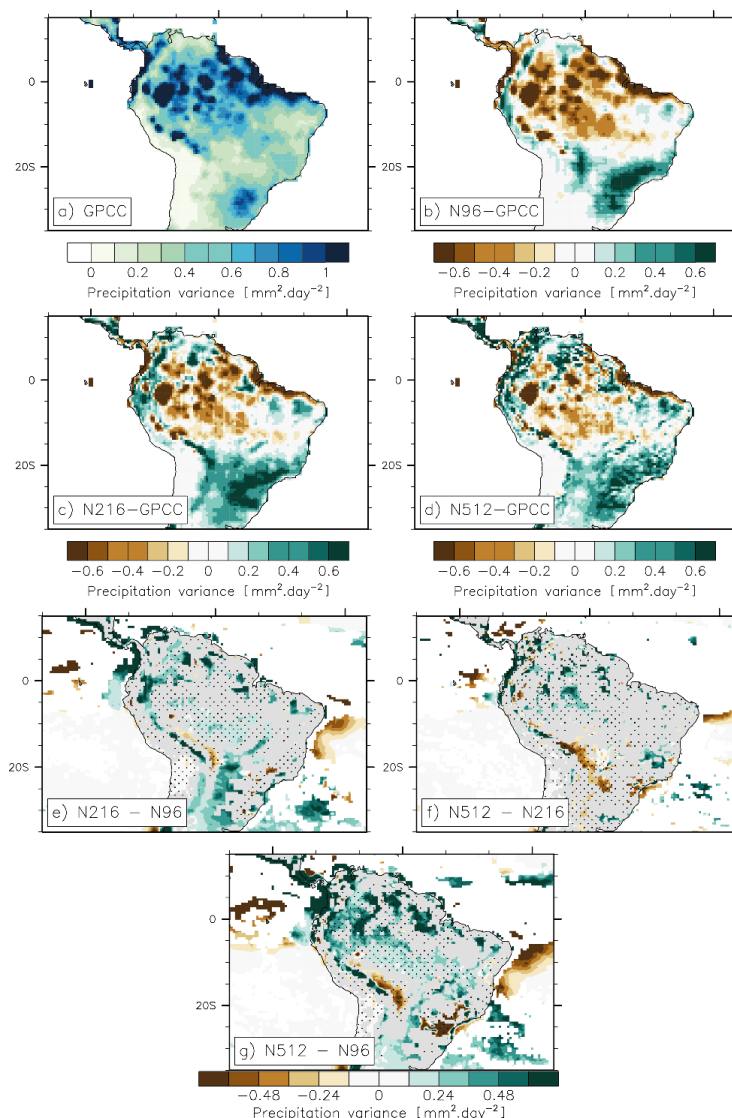
791 **Figure 3:** Ensemble-mean N216-N96 difference in (a) DJF, (d), MAM, (g) JJA and (j) SON precipitation
792 (mm.day⁻¹). (b), (e), (h) and (k), as in (a), (d), (g) and (j) but for N512-N216. (c), (f), (i) and (l), as in (a),
793 (d), (g) and (j) but for N512-N96. Differences are shown when statistically different to zero, according to a
794 Student's t-test and a 95% confidence level.

795

796

797

798

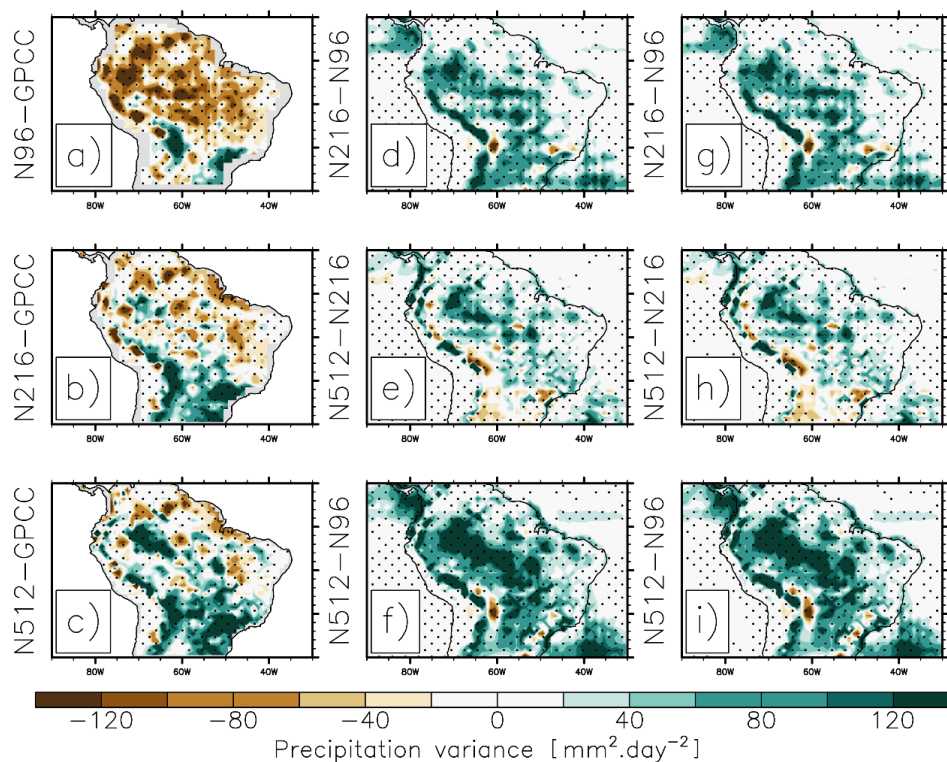


799

800 **Figure 4:** (a) Observed annual-mean precipitation variance (GPCC; $\text{mm}^2.\text{day}^{-2}$), as computed over the
801 period 1982–2014. A linear trend is removed. Bias in annual-mean precipitation variance in (b) N96 (i.e.
802 N96–GPCC), (c) N216 (i.e. N216–GPCC) and (d) N512 (i.e. N512–GPCC). (e) N216–N96, (f) N512–N216
803 and (g) N512–N96 differences in annual-mean precipitation variance. On (b), (c) and (d), biases are shown
804 when all three members produces a bias that is significant according to a f-test and a 95% confidence level.
805 On (e), (f) and (g), stippling indicates that the bias is improved at the higher than at the lower resolution.

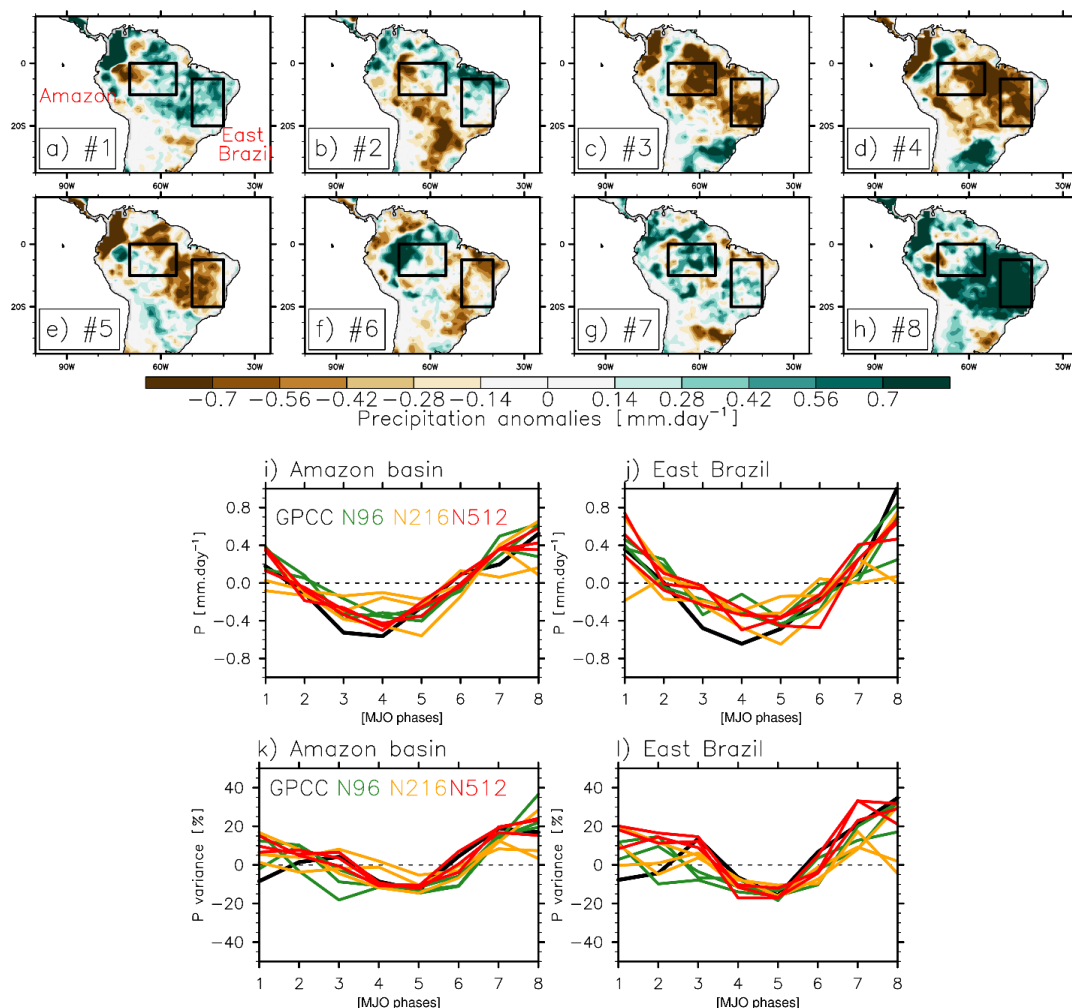
806

807



808

809 **Figure 5:** (Left row) Bias in daily precipitation variance ($\text{mm}^2.\text{day}^{-2}$) for (a) N96 (i.e. N96-GPCC), (b) N216
810 (i.e. N216-GPCC) and (c) N512 (i.e. N512-GPCC) simulations, over the DJF period. Seasonal cycle and
811 linear trend are removed prior to computing variance. Differences in daily precipitation variance ($\text{mm}^2.\text{day}^{-2}$)
812 for (d) N216-N96, (e) N512-N216 and (f) N512-N96. (g), (h) and (i), as in (d), (e) and (f) but for P-E
813 (precipitation minus evaporation) variance.



814

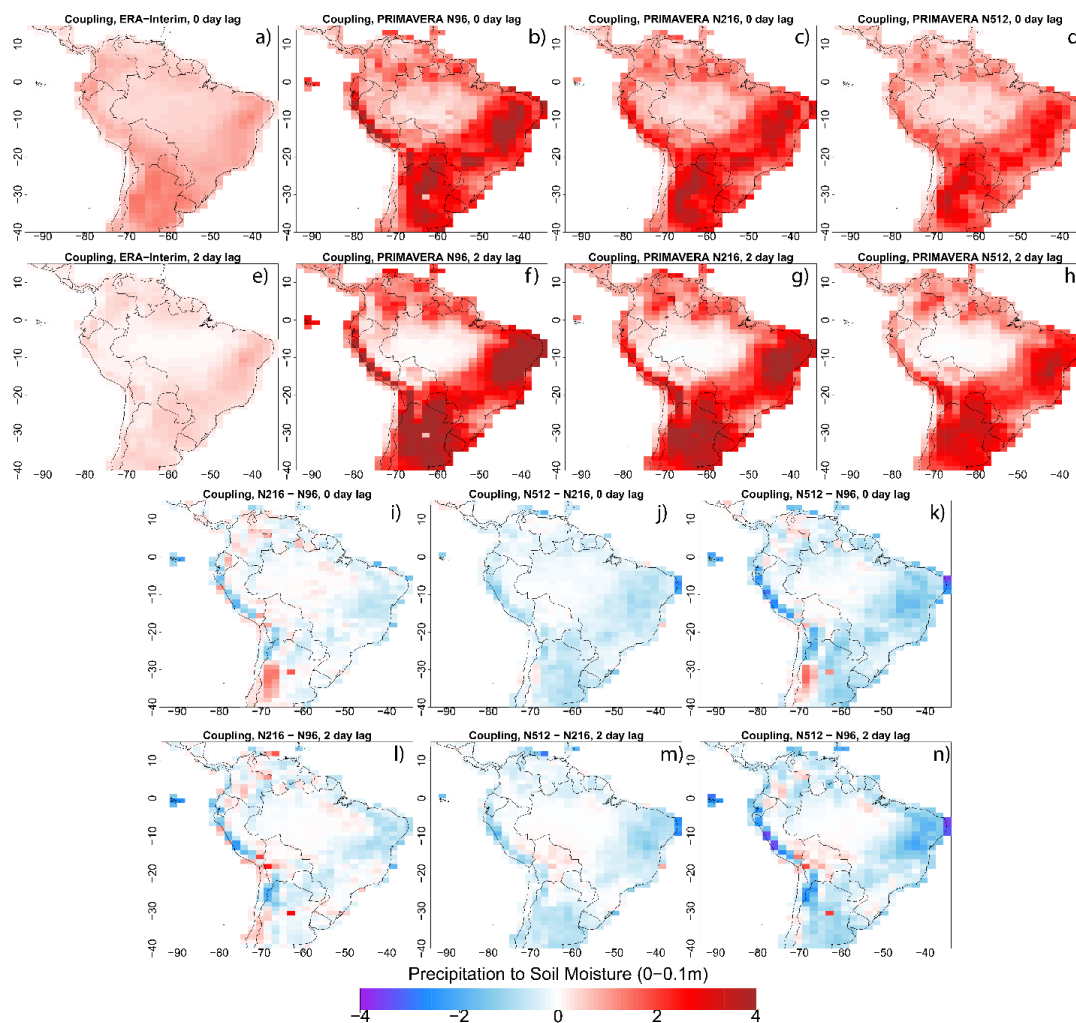
815 **Figure 6:** Observed impacts of Madden-Julian Oscillation phase (a) 1, (b) 2, (c) 3, (d) 4, (e) 5, (f) 6, (g) 7
 816 and (h) 8 on precipitation (GPCC and NCEP for the RMM index; $\text{mm}\cdot\text{day}^{-1}$). Precipitation anomalies
 817 ($\text{mm}\cdot\text{day}^{-1}$), associated with each phase of the Madden-Julian Oscillation, relative to the period 1982-2014,
 818 and averaged over the (i) Amazon Basin and (j) East Brazil (see the box on (a)), for observation (black),
 819 N96 (green), N216 (orange) and N512 (red). (k) and (l), as in (i) and (j) but for precipitation variance, in
 820 percent (%) of the precipitation variance over the period 1982-2014.

821

822

823

824



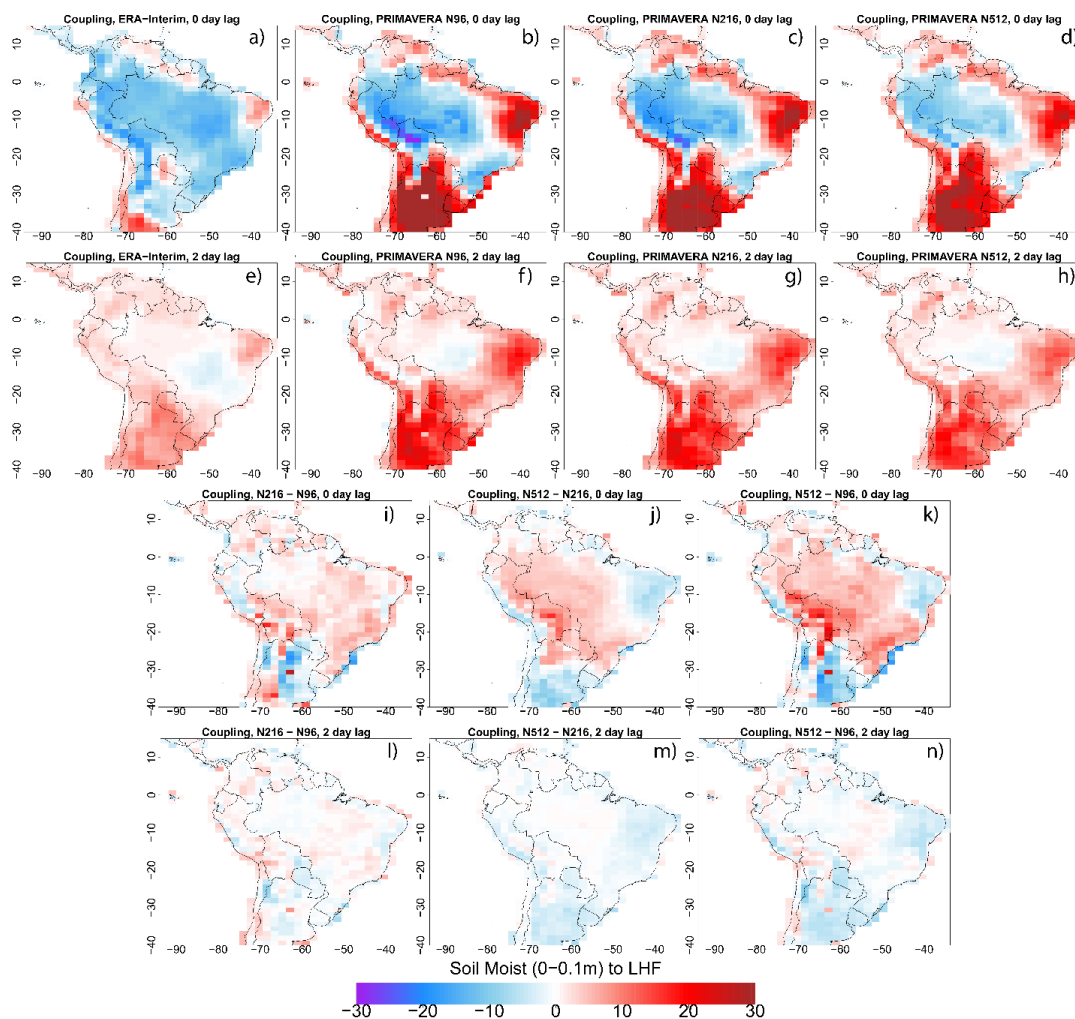
825

826 **Figure 7:** (a) Observed (ERA-Interim) and (b) N96, (c) N216 and (d) N512 Coupling strength ($r_{a,b\sigma_b}$)
 827 between daily precipitation and soil moisture (in the top 0.1m of soil) during the southern summer
 828 wet season (DJF), over the period 1979-2014. 2-day time lag (i.e. the soil situation 2 days after
 829 precipitation) for (e) ERA-Interim, (f) N96, (g) N216 and (h) N512. (i) N216-N96, (j) N512-N216
 830 and (k) N512-N96 coupling strength. (l), (m), (n), as for (i), (j) and (k) but with a 2-day time lag
 831 between precipitation and soil moisture.

832

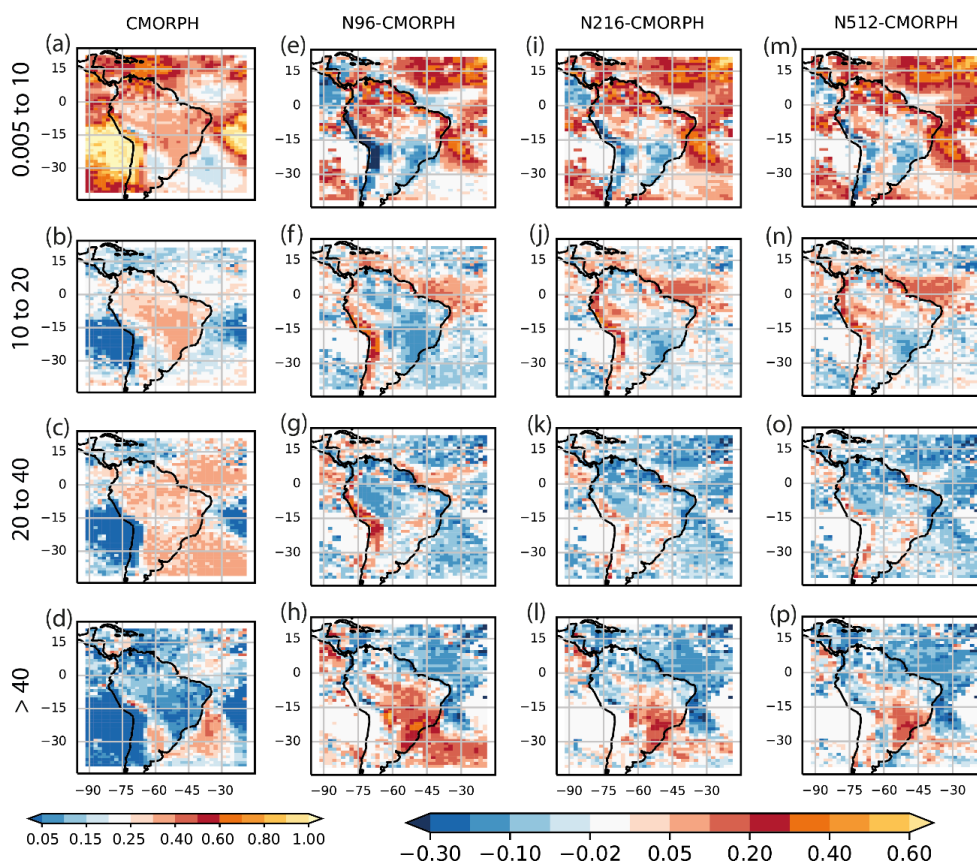
833

834



835

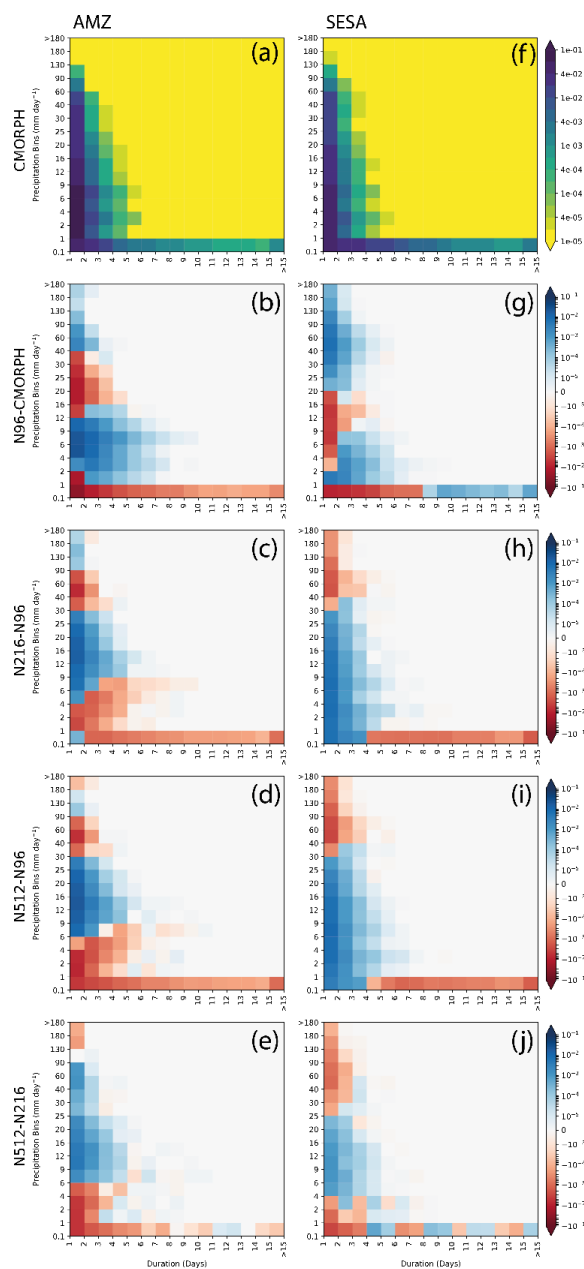
836 Figure 8: As in Figure 7 but for the coupling strength between daily soil moisture (in the top 0.1m of
837 soil) and latent heat flux (LHF).



838
839

840 **Figure 9:** Fractional contribution to the total precipitation from ranges of intensity bins shown in the labels
841 above each panel for CMORPH (a-d) (the sum of each column is unity). Differences in the fractional
842 contributions compared against CMORPH for N96 (e-f), N216 (i-l) and N512 (m-p) all on the N96 common
843 grid. The four ranges of intensity bins are (first row) 0.005 to 10 mm/day, (second row) 10 to 20 mm/day,
844 (third row) 20 to 40 mm/day and (last row) >40 mm.day⁻¹.

845
846

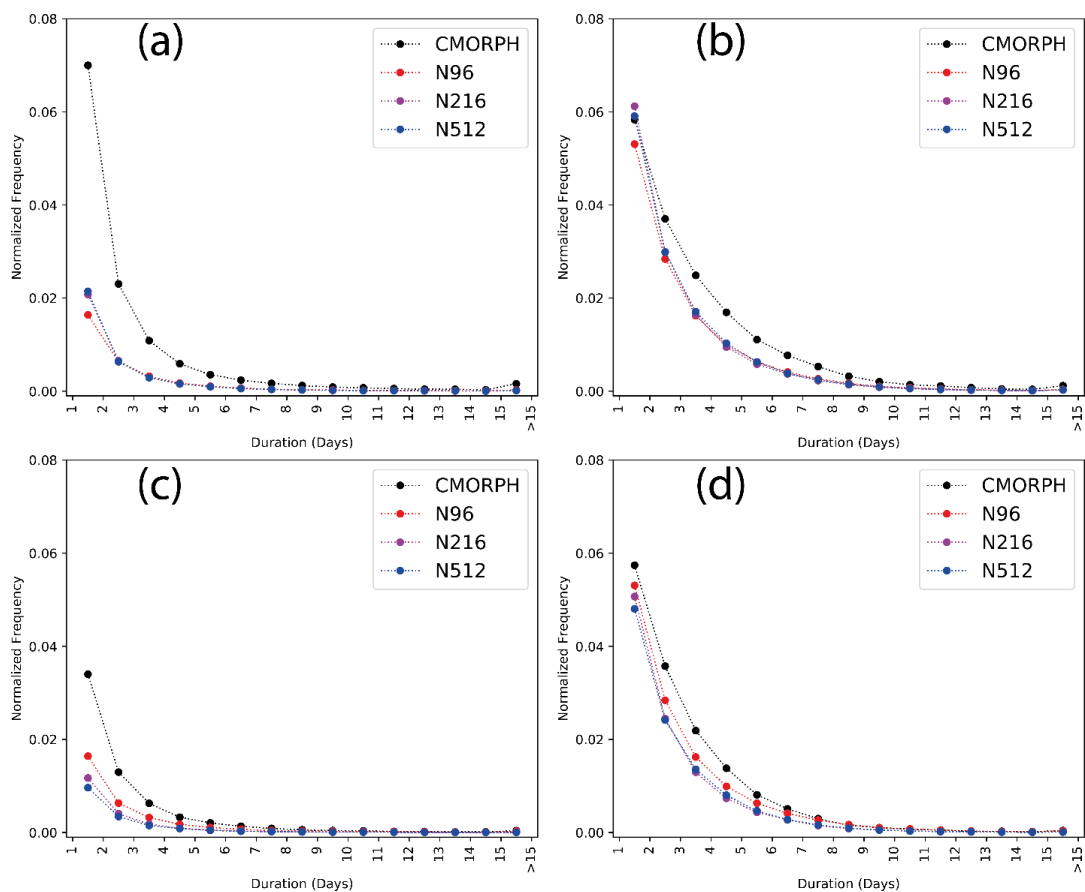


847

848 **Figure 10:** Two-dimensional histograms of binned precipitation lasting for each duration bin, aggregated
849 over all grid points and normalized by the number of spatial and temporal points in each dataset for (a)
850 CMORPH for the AMZ region at N96 grid. Differences between the two-dimensional histograms for (b)
851 N96 minus CMORPH; (c) N216 minus N96; (d) N512 minus N96 and (e) N512 minus N216 computed on
852 the common N96 grid. (f-j) is same as (a-e) but for the SESA region.



853

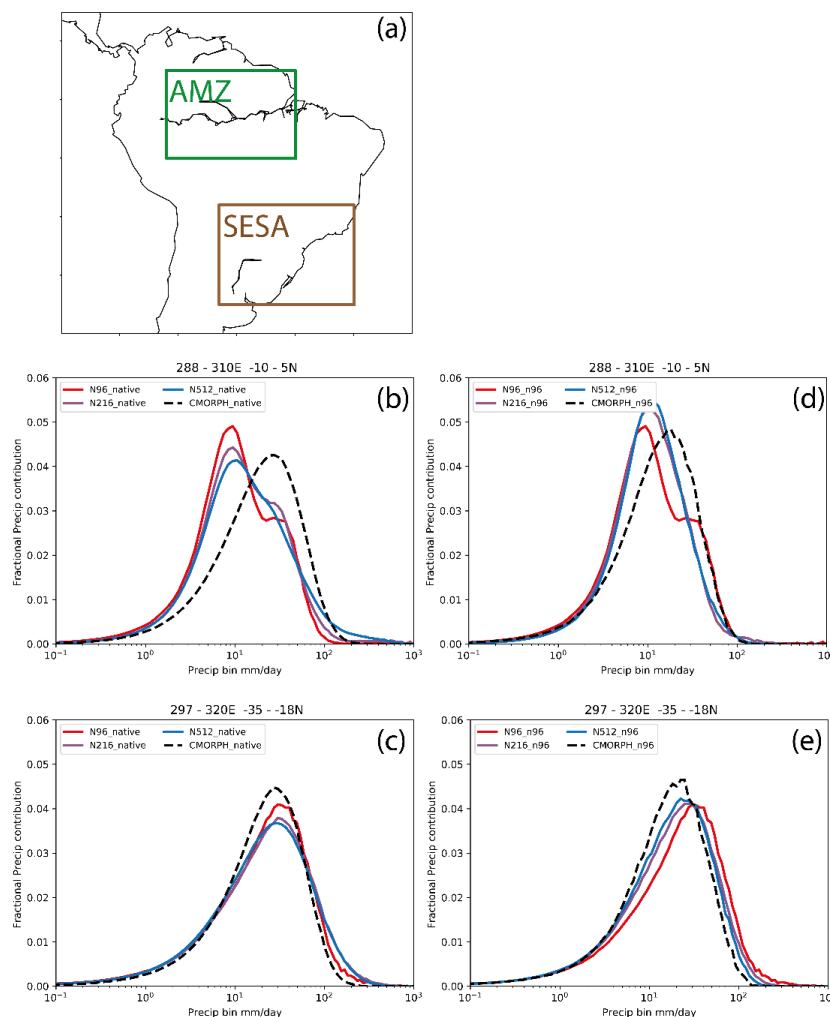


854

855 **Figure 11:** Histograms of dry days (with precipitation less than 0.1 mm day^{-1}) lasting for each duration bin,
856 aggregated over all grid points and normalized by the number of spatial and temporal points in each dataset
857 (a) Amazon and (b) SESA at native resolution for all datasets. (c-d) is same as (a-b) but for datasets on the
858 common N96 grid.

859

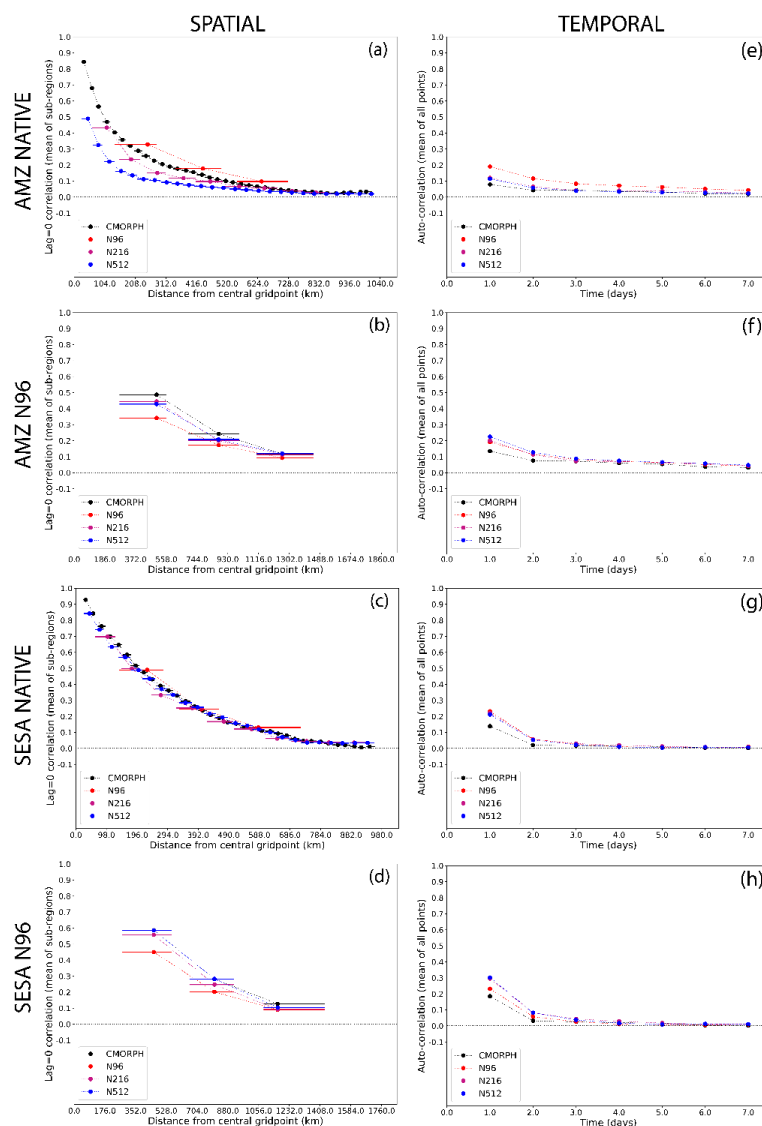
860



861

862 **Figure 12:** (a) Subregions used in our study (i) the Amazon region (AMZ; green box; 10°S – 5°N; 72°W –
863 50°W) and (ii) the southeast South America region (SESA; brown box; 35°S – 18°S; 63°W – 40°W).
864 Histograms of the average precipitation contributions to the total precipitation from each precipitation bin
865 for CMORPH and all simulations on their native grids (b) AMZ and (c) SESA. (d-e) is same as (b-c) but at
866 96 grid.

867



868

869 **Figure 13:** (a) metric of the spatial scale of daily precipitation (at native resolution), computed by dividing
 870 the analysis domain into 1500 km x 1500 km sub-regions and calculating the mean lag-0 correlation
 871 between the central grid point and all grid points within each distance bin (which are 1 delta x wide, starting
 872 from 0.51x) away from the central grid point, then averaging the correlations over all sub-regions in AMZ;
 873 (e) metric of the temporal scale of daily precipitation, computed as the autocorrelation at each point,
 874 averaged over all points AMZ. The horizontal lines in (a-d) show the range of distances spanned by each
 875 distance bin; the filled circle is placed at the median distance. For clarity, we omit the correlations for zero
 876 distance and zero lag, which are 1.0 by definition. (b and f) same as (a and c) respectively for all datasets
 877 on the N96 grid; (c-d and g-h) same as (a-b and e-f) respectively but for SESA.